Tip-Sample Contact Lateral Forces in Tapping and Contact Mode Operation of the Atomic Force Microscope

by

Amro M. Farid

Submitted to the Mechanical Engineering
in partial fulfillment of the requirements for the degree of

Bachelor of Science

at the

MASSACHUSETTS INSTITUTE OF TECHNOLOGY

June 2000

Author .....
Mechanical Engineering
May 22, 2000

Certified by .....
Kamal Youcef-Toumi
Professor
Thesis Supervisor

Accepted by .....
Professor Ernest G. Cravalho
Chairman, Undergraduate Thesis Committee

Tip-Sample Contact Lateral Forces in Tapping and Contact Mode Operation of the Atomic Force Microscope

by

Amro M. Farid

Submitted to the Mechanical Engineering
on May 22, 2000, in partial fulfillment of the
requirements for the degree of
Bachelor of Science

Abstract

This thesis sets out to find the relative magnitude of contact and tapping mode lateral surface forces in the Atomic Force Microscope. First, it describes the uses and operation of the instrument and follows with an explanation of the need for such a study. The vertical dynamics of the AFM are then derived. A review of the current status of the literature on contact mode lateral surface force models is then presented. The Johnson-Woodhouse model is chosen and expanded to include tapping mode operation of the AFM. Finally, simulations are performed by combining the vertical dynamics of the AFM with the newly developed lateral surface force model. Simulation results indicate that contact mode surface forces are always greater than tapping mode surface forces. Tapping mode surface forces are also found to depend on scan rate.

Thesis Supervisor: Kamal Youcef-Toumi
Title: Professor

Acknowledgments

I would like to thank Professor Kamal Youcef-Toumi for posing the question of surface interactions in the Atomic Force Microscope, for it has gripped my interest and thrilled my curiosity. The opportunity to work on this project has improved my understanding of nanoscale surface forces, modeling techniques, modal analysis, Matlab/Simulink and numerical solution methods. I would like to further thank Professor Youcef-Toumi for advising me through this year long project and for allowing me to work on the Mechatronics Research Laboratory's computers which were tied up in countless hours of simulation.

I would like to thank Osamah El Rifai for stimulating conversations on the dynamics of the Atomic Force Microscope. His experienced opinions served to guide many of my research initiatives. I would like to further thank him for being a second reader of my thesis, and giving me much feedback on it.

Many people in my personal life have helped me in producing this document. Eric Liu, Ramy Abu-Khalil and Elicia Anderson not only provided a mechanical engineering forum in which I could 'bounce' my ideas but also provided moral support and encouragement through many sleepless nights. I thank Mr. James Soltman and Mr. Kevin McLaughlin for virtuosicly teaching my first courses in Physics and Chemistry. Lastly, I thank my father Mohsen Farid for sparking my interest in physics at a very young age.

Contents

List of Figures

Chapter 1

Introduction

1.1 Background

The invention[1] of the atomic force microscope (AFM) in 1986 significantly improved the ability to scan surfaces at the nanometer scale. By using the deflection of a fine tipped cantilever, surface forces can be measured to determine the surface profile. Prior to the AFM, scanning tunneling microscopes were used to achieve nanoscale resolution. Scanning tunneling microscopy, however, was limited to just conductive materials because it measured tunneling current. By measuring surface forces, the AFM provided a unique benefit in its ability to scan a much greater variety of materials [2].

This variety has opened up a wealth of research in biology, optics, material science and tribology. In biology, AFM scans have been particularly useful. It has shown the interactions of living cells. On a much smaller scale, single strands of DNA have been characterized [3] and the docking mechanism of complementary antibody and antigen pairs has been demonstrated [4][1]. In the field of optics, surface characterization is becoming increasingly important as lense tolerances decrease in efforts to minimize scattering. The AFM has also shown direct applications in the contact lense industry. Lense life can be improved and surface defects minimized when the AFM is used as a quality control apparatus. The field of material science has also benefited greatly from a great deal of experimental data provided by the AFM. At first, the AFM was used for morphology studies, but was later used to investigate the nanostructure of many polymers [5]. Also due to the direct mechan-

[1]Color images of some AFM scans can be found at http://www.di.com

ical contact, the AFM can give insights into the nanomechanics of the material [6]. It is these nanomechanics that has opened the field of tribology to include 'nanotribology'. The cantilever deflection in horizontal directions allow for force measurements with a resolution never before achieved. These measurements can be used to make deductions on nanoscale friction. Experimental measurement at the atomic scale has allowed the field of tribology to aggressively pursue the true physical basis for friction.

1.2 Functionality

Atomic force microscopy has had more success than other microscopy techniques because of its superior design. Figure 1-1 shows a schematic of a typical atomic force microscope. Two

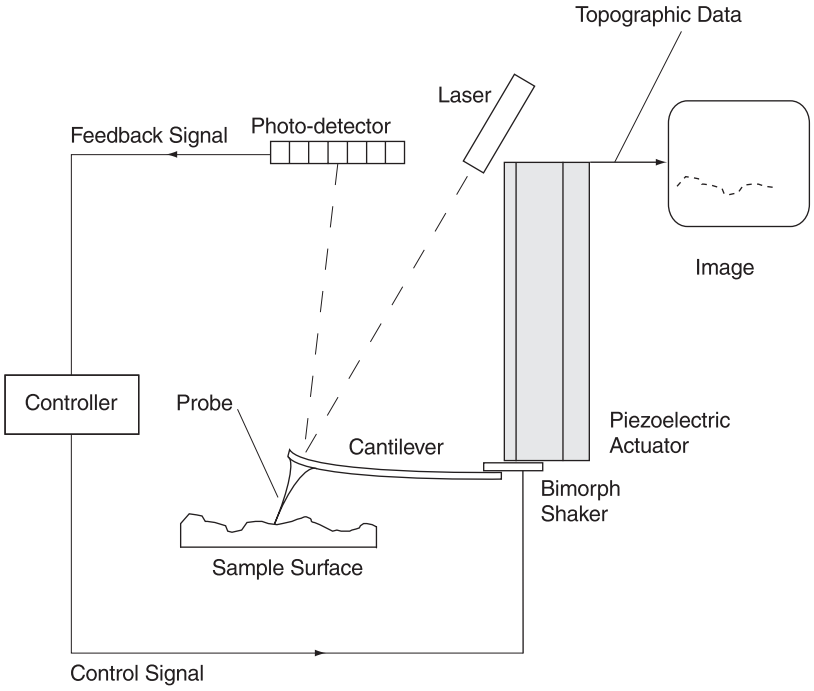

Figure 1-1: A Schematic of the Atomic Force Microscope

components make up the principle parts of the atomic force microscope. A piezoelectric tube acts as an electrically controlled actuator in the vertical direction. By bending the piezoelectric tube, it also provides a constant lateral velocity for scanning. The AFM cantilever is attached to the piezoelectric tube. It is often made of silicon and coated with a reflective coating of gold. Its tip is very sharp; often having a radius of curvature of ten

nanometers. Such a sharp asperity allows for a very fine resolution of the scanned surface.

Prior to scanning, the piezoelectric tube is set to a voltage that corresponds to a particular cantilever deflection. Once scanning begins, acquisition of a surface image occurs by controlling this deflection. An infrared laser shines light at the cantilever's reflective surface. A planar photodetector measures the position and intensity of the reflected light beam. The position is dependant upon the cantilever's deflection which is in turn dependant upon the force on the cantilever tip and the surface profile. The photodetector output is then used as a feedback signal which is sent to a controller that attempts to maintain the deflection on the cantilever by sending control signals to actuate vertically the piezoelectric tube. The voltage of the piezoelectric tube is used to construct an image of the surface.

This mode of operation is called contact mode and was the first method of operation of the atomic force microscope. As AFM technology matured, it was found that for some applications contact mode resulted in heavy deformation and severe damage to the sample surface. This results in a diminished image accuracy. To address this issue, a tapping mode of operation was developed. A bimorph shaker was added to the end of the piezoelectric tube. Its purpose is to sinusoidally drive the cantilever vertically near its natural frequency. The cantilever for most of its amplitude remains well above the sample surface, but touches the sample very briefly. As tapping mode scan is performed, the cantilever's amplitude is measured for feedback. A smaller amplitude results from a peak in the sample surface causing an upward motion of the piezoelectric tube.

1.3 Friction Questions

The primary advantage of tapping mode is that it limits the amount of time that the cantilever tip is in contact with the surface, while retrieving a similar amount of data about it. This, however, does not lead to any direct conclusions about the relative magnitude of asperity to surface forces in both modes. Certainly, a combination of tapping mode conditions can lead to normal forces that are equal or greater than contact mode normal forces. The primary difference between tapping and contact mode is the relative duration in which the sample and asperity are exposed to these surfaces.

As there are questions with the relative magnitude of normal forces in both modes of operation, there are questions on the relative magnitude of lateral surface forces as well.

Similar normal forces should result in similar horizontal forces. At the same time, similar lateral forces should result in similar horizontal deflections of the cantilever. It is unclear as to whether the brief contact time would allow for the full magnitude of this deflection. The elastic properties of the AFM cantilever might also play a role in the magnitude of there forces. The magnitude of the lateral surface force effectively becomes one type of measuring the accuracy of the scan and how well the sample is preserved after measurement.

1.4 Overview of Approach

This thesis will attempt to answer these questions on horizontal surface forces in the atomic force microscope. In particular, how are they related to normal force at the nanoscale? Is the relationship different in tapping and contact modes? Many steps, however, need to be taken before these questions can be properly answered. The normal force on the cantilever tip will depend on the dynamics of the AFM. Chapter 2 will derive the equations of motion of the AFM in both tapping mode and contact modes. Once this has been done, the thesis shifts its focus to understand nanoscale surface interactions. A strong understanding of how horizontal forces occur and how they depend upon normal force, position, velocity among other AFM properties is required. Chapter 3 conducts a literature review of recent models on the nature of surface forces in the AFM. Chapter 4 chooses a single model from those presented. It ensures that the model applies to both tapping and contact mode. Chapter **??** brings the AFM dynamics together with the model into a single Simulink model.

Chapter 2

Atomic Force Microscope Dynamics

2.1 Modeling Overview

Later chapters will show that horizontal surface forces at the nanoscale depend on the position and velocity of the probe. In essence, tip-sample interactions in the AFM is coupled to the rest of the AFM system dynamics. Attempts to understand these interactions in the AFM, therefore, require a good understanding of the AFM in both contact and tapping modes. This chapter will explain the AFM system dynamics so that a greater understanding of AFM nanoscale surface interactions are achieved later.

As discussed in Chapter 1, the AFM consists of a piezoelectric tube, a bimorph shaker, and a cantilever beam that have dynamics in horizontal and vertical directions. By exploring the dynamics in the vertical direction, this chapter will differentiate between tapping and contact mode. The piezoelectric tube and the cantilever are independently modeled as mass-spring-dashpot systems. The bimorph shaker acts as a displacement source embedded between the two systems. Figure 2-1 shows a graphical representation of the modeled system.

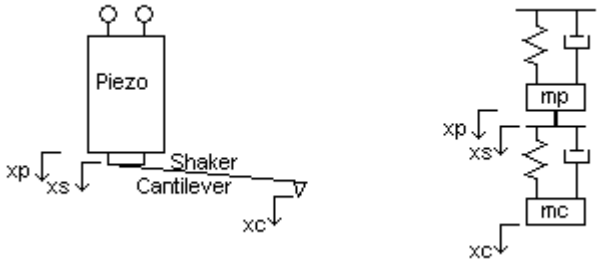

Figure 2-1: Double Mass-Spring-Dashpot Analogy of AFM System

2.2 Piezoelectric Tube Dynamics

Ohara and Youcef-Toumi [7] state the constitutive relation for piezoelectric tubes.

$$\begin{bmatrix} \epsilon_z \\ D_r \end{bmatrix} = \begin{bmatrix} 1/E_p & d_{31} \\ d_{31} & C_p \end{bmatrix} \begin{bmatrix} \sigma_z \\ E_r \end{bmatrix} \tag{2.1}$$

The piezoelectric tube's equation of motion is then found through force balance [7];

$$\rho_p A_p \ddot{z}_p + b_p \dot{z}_p - A_p E_p \frac{\partial^2 z_p}{\partial^2 l_p} = \frac{A_p E_p d_{31}}{(R_o - R_i)} V_{zp} \delta(l_p - L_p) \tag{2.2}$$

Appendix A contains a list of variables and symbol definitions. This partial differential equation can be solved by applying the method of separation of variables. The solution is a product of two terms that either depend on time or position superimposed for every applicable vibration mode.

$$z_p(l_p, t) = \sum_{n=1}^{\infty} \Phi_{pn}(l_p) T_{pn}(t) \tag{2.3}$$

The boundary conditions are described as fixed at the top and determined by force balance at the bottom. Mathematically,

$$z_p = 0|_{lp=0}$$

$$M_{hold} \frac{\partial^2 z_p}{\partial^2 t^2} + b_p \frac{\partial z_p}{\partial t} + A_p E_p \frac{\partial z_p}{\partial l_p} = \frac{A_p E_p d_{31}}{R_o - R_i} V_{zp}|_{lp=Lp} \tag{2.4}$$

They give an infinite number of sinusoidal mode shapes Φ_{pn} where B_n is an arbitrary constant assumed to equal one and $\varphi = \sqrt{\frac{E_p}{\rho_p}}$.

$$\Phi_{pn} = B_n \sin\left(\frac{\omega_{pn} l_p}{\varphi}\right) \tag{2.5}$$

The natural frequencies ω_{pn} are found by numerically solving the transcendental equation below.

$$\frac{\omega_{pn} L_p}{\varphi} \tan\left(\frac{\omega_{pn} L_p}{\varphi}\right) = \frac{\rho_p A_p L_p}{M_{hold}} \tag{2.6}$$

The time dependent portion of the solution, $T_{pn}(t)$, found in Equation (2.3) can be found by solving a second order ordinary differential equation that describes a mass-spring-dashpot system;

$$m_{pn}\ddot{T}_{pn} + c_{pn}\dot{T}_{pn} + k_{pn}T_{pn} = Q_{pn} \tag{2.7}$$

It will be assumed that the complete piezoelectric tube response will be dominated by just its first mode response. The first mode modal mass is,

$$m_p = \int_0^{L_p} \rho_p A_p \Phi_p^2(l_p) dl_p + \int_0^{L_p} M_{hold} \Phi_p^2(l_p) \delta(l_p - L_p) dl_p \tag{2.8}$$

Substituting for the first mode shape and integrating over the length of the piezoelectric gives,

$$m_p = \rho_p A_p \left[\frac{L_p}{2} - \frac{\varphi}{4\omega_p} \sin\left(\frac{2\omega_p L_p}{\varphi}\right)\right] + M_{hold} \sin^2\left(\frac{\omega_p L_p}{\varphi}\right) \tag{2.9}$$

The modal damping for the first mode is proportional to the cantilever portion of the modal mass. The constant b_p is tuned to agree with experimental results.

$$c_p = b_p \left[\frac{L_p}{2} - \frac{\varphi}{4\omega_p} \sin\left(\frac{2\omega_p L_p}{\varphi}\right)\right] \tag{2.10}$$

The modal stiffness for the first mode comes from the definition of the natural frequency for a mechanical system.

$$k_p = m_p \omega_p^2 \tag{2.11}$$

The only forces on the piezoelectric tube are due to the imposed voltage. The modal excitation term is,

$$Q_p = \int_0^{L_p} \Phi_p \frac{A_p E_p d_{31}}{(R_o - R_i)} V_{zp} \delta(z - L_p) dl_p \tag{2.12}$$

Substituting for the first mode shape and integrating over the length of the piezoelectric gives,

$$Q_p = K_{pv} V_{zp} \tag{2.13}$$

Where K_{pv} is a constant defined as,

$$K_{pv} = \frac{A_p E_p d_{31}}{(R_o - R_i)} \sin\left(\frac{\omega_p L_p}{\varphi}\right) \tag{2.14}$$

With the mass, damping, stiffness, and excitation terms defined, the piezoelectric tube's dynamics are fully defined. The focus can now shift to the dynamics of the cantilever beam.

2.3 Cantilever Beam Dynamics

Describing the dynamics of the AFM cantilever requires special care. Because it is attached to two dynamic components, the shaker and the piezoelectric tube, a relative displacement coordinate system is introduced. The displacement of the shaker, z_s, is relative to the piezoelectric tube, and the displacement of the cantilever, z_c, is in turn relative to the bimorph shaker. Neglecting the bending moment due to tangential forces, the equation of motion of the cantilever is found through force balance [8]. The following derivation will be for the general tapping mode case. Contact mode dynamics are a degenerate form of tapping mode dynamics.

$$\rho A_c \frac{\partial^2 (z_c + z_s + z_p)}{\partial t^2} + b_{cz} \frac{\partial (z_c + z_s + z_p)}{\partial t} + E_c I \frac{\partial^4 z_c}{\partial l_c^4} = \left[F_n - b_s \frac{\partial (z_c + z_s + z_p)}{\partial t} \right] \delta(l_c - L) \tag{2.15}$$

This form of the partial differential equation is not conducive to a solution. Bringing the shaker and piezoelectric's acceleration and velocity terms to the right hand side gives:

$$\rho A_c \ddot{z}_c + b_{cz} \dot{z}_c + E_c I \frac{\partial^4 z_c}{\partial l_c^4} = [F_n - b_s(\dot{z}_c + \dot{z}_s + \dot{z}_p)]\delta(l_c - L) - \rho A_c \ddot{z}_s - \rho A_c \ddot{z}_p - b_{cz} \dot{z}_s - b_{cz} \dot{z}_p \tag{2.16}$$

As in the previous section, the partial differential equation is solved by the method of separation of variables.

$$z_c(l_c, t) = \sum_{n=1}^{\infty} \Phi_n(z) T_n(t) \tag{2.17}$$

There are four boundary conditions. The end of the cantilever attached to the bimorph shaker has no displacement and a horizontal slope. The tip of the cantilever has no shear force or bending moment. Mathematically, this can be stated as,

$$\begin{aligned} z_c = 0|_{lc=0} \qquad & \frac{\partial z_c}{\partial l_c} = 0|_{lc=0} \\ \frac{\partial^2 z_c}{\partial^2 l_c} = 0|_{lc=L} \qquad & \frac{\partial^3 z_c}{\partial^3 l_c} = 0|_{lc=L} \end{aligned} \tag{2.18}$$

The boundary conditions determine the following infinite series of mode shapes,

$$\Phi_n(l_c) = -\sin(\lambda_{cn} l_c) + \sinh(\lambda_{cn} l_c) + \alpha_n \left(\cos(\lambda_{cn} l_c) - \cosh(\lambda_{cn} l_c)\right) \tag{2.19}$$

The constant α_n is defined with a combination of four trigonometric functions,

$$\alpha_n = \left(\frac{\sin(\lambda_{cn} L) + \sinh(\lambda_n L)}{\cos(\lambda_{cn} L) + \cosh(\lambda_{cn} L)}\right) \tag{2.20}$$

The wave number, λ_{cn}, is found by solving the transcendental equation below:

$$\cos(\lambda_{cn} L)\cosh(\lambda_{cn} L) + 1 = 0 \tag{2.21}$$

The time dependent portion of the solution, T_n to the PDE can be found by solving a second order ordinary differential equation that describes a mass- spring-dashpot system.

$$m_{cn}\ddot{T_n} + b_n \dot{T_n} + k_{zn} T = Q_n \tag{2.22}$$

As in the previous section, it will be assumed that the cantilever response will be dominated by its first mode of vibration. The modal mass of the first mode is given by,

$$m_c = \int_0^L \rho A_c \Phi(l_c) dl_c \tag{2.23}$$

The damping term, b_{cz}, is tuned to experimental data, and the stiffness term is given by,

$$k_{cz} = E_c I \int_0^L \left(\frac{\partial^2 \Phi(l_c)}{\partial x^2}\right)^2 dl_c \tag{2.24}$$

All the external forces can be lumped into a single excitation term.

$$Q = \int_0^L \Phi \left[(F_n - b_{cz}\dot{z}_p - b_{cz}\dot{z}_s)\delta(l_c - L) - \rho A_c \ddot{z}_p - \rho A_c \ddot{z}_s - b_{cz}\dot{z}_p - b_{cz}\dot{z}_s \right] dl_c \tag{2.25}$$

The excitation can be rewritten in an easily usable form,

$$Q = -(\rho A_c \ddot{z}_p + \rho A_c \ddot{z}_s + b_{cz}\dot{z}_p + b_{cz}\dot{z}_s) \int_0^L \Phi \, dl_c + \Phi(L)[F_n - b_s(\dot{z}_p + \dot{z}_s)] \tag{2.26}$$

The excitation term reveals the coupled nature of Equation (2.22). Before solving it, the ODE stated in Equation (2.7) needs to be put in a more suitable form.

$$\ddot{z}_p = -\frac{c_p}{m_p}\dot{z}_p - \frac{k_p}{m_p}z_p + \frac{K_{pv}}{m_p}V_{zp} \tag{2.27}$$

Substituting this result into Equation (2.22) gives,

$$\begin{aligned} m_c\ddot{T} + b_{cz}\dot{T} + k_z T &= \left[\rho A_c \left(\frac{c_p}{m_p}\dot{z}_p + \frac{k_p}{m_p}z_s - \frac{k_{pv}}{m_p}V_{zp} \right) - \rho A_c \ddot{z}_s - b_{cz}\dot{z}_p - b_{cz}\dot{z}_s \right] \int_0^L \Phi \, dl_c \\ &\quad + \Phi^2(L)[F_n - b_s(\dot{z}_p + \dot{z}_s)] \end{aligned} \tag{2.28}$$

This ODE can be written so that all modal displacements, velocities, and accelerations are replaced with their real equivalents.

$$\begin{aligned} m_c\ddot{z}_c + b_{cz}\dot{z}_c + k_z z_c &= \left[\rho A_c \left(\frac{c_p}{m_p}\dot{z}_p + \frac{k_p}{m_p}z_p - \frac{k_p v}{m_p}V_{zp} \right) - \rho A_c \ddot{z}_s - b_{cz}\dot{z}_p - b_{cz}\dot{z}_s \right] \Phi(L) \int_0^L \Phi \, dz \\ &\quad + \Phi^2(L)[F_n - b_s(\dot{z}_p + \dot{z}_s)] \end{aligned} \tag{2.29}$$

The ordinary differential equations stated in Equations (2.27) and (2.29) fully describe the dynamics of the atomic force microscope system. Section 2.4 focuses on describing all of the equations in a coherent state space representation.

2.4 State Space Representation of AFM System

The equations of the first two sections of this chapter can now be unified into a state-space representation. The standard form is

$$\dot{X} = AX + Bu \tag{2.30}$$

$$y = CX + Du \tag{2.31}$$

Using the cantilever tip displacement and velocity, and the piezoelectric tube displacement and velocity as states, the state space form in Equation (2.30) can be expanded to;

$$\begin{bmatrix} \dot{z}_c \\ \ddot{z}_c \\ \dot{z}_p \\ \ddot{z}_p \end{bmatrix} = \begin{bmatrix} 0 & 1 & 0 & 0 \\ -\frac{k_{cz}}{m_c} & -\frac{b_{cz}}{m_c} & \frac{\rho A_c k_p \Phi}{m_c m_p} \int_0^L \Phi \, dl_c & \frac{\Phi}{m_c}\left(\rho A_c \frac{c_p}{m_p} - b_{cz}\right) \int_0^L \Phi \, dl_c - \frac{\Phi^2 b_s}{m_c} \\ 0 & 0 & 0 & 1 \\ 0 & 0 & -\frac{k_p}{m_p} & -\frac{c_p}{m_p} \end{bmatrix} \begin{bmatrix} z_c \\ \dot{z}_c \\ z_p \\ \dot{z}_p \end{bmatrix}$$
$$+ \begin{bmatrix} 0 & 0 & 0 & 0 \\ -\frac{\rho A_c K_{pv} \Phi}{m_c m_p} \int_0^L \Phi \, dl_c & -\frac{\Phi^2}{m_c} & \frac{\rho A_c \Phi}{m_c} \int_0^L \Phi \, dl_c & -\frac{b_{cz} \Phi}{m_c} \int_0^L \Phi \, dl_c - \frac{\Phi^2 b_s}{m_c} \\ 0 & 0 & 0 & 0 \\ \frac{K_{pv}}{m_p} & 0 & 0 & 0 \end{bmatrix} \begin{bmatrix} V_{zp} \\ F_n \\ \ddot{z}_s \\ \dot{z}_s \end{bmatrix} \tag{2.32}$$

The Atomic Force Microscope uses the cantilever displacement for feedback in both tapping and contact mode. Equation (2.31) can then be written as,

$$z_c = \begin{bmatrix} 1 & 0 & 0 & 0 \end{bmatrix} \begin{bmatrix} z_c \\ \dot{z}_c \\ z_p \\ \dot{z}_p \end{bmatrix} \tag{2.33}$$

A non-dimensional notation is now introduced.

$$\begin{array}{rclrclrcl} q & = & z_c/(\Phi D_m) & q_p & = & z_p/D_m & q_s & = & z_s/D_m \\ \dot{q} & = & \dot{z}_c/(\Phi D_m \omega_{cz}) & \dot{q_p} & = & \dot{z_p}/(D_m \omega_{cz}) & \dot{q_s} & = & \dot{z_s}/(D_m \omega_{cz}) \\ \ddot{q} & = & \ddot{z}_c/(\Phi D_m \omega_{cz}^2) & \ddot{q_p} & = & \ddot{z_p}/(D_m \omega_{cz}^2) & \ddot{q_s} & = & \ddot{z_s}/(D_m \omega_{cz}^2) \\ \bar{V_{zp}} & = & V_{zp} & & & & \bar{F_n} & = & F_n/(2\pi\gamma R_a) \end{array} \tag{2.34}$$

The non-dimensional form improves feasibility. A dimensional form causes numbers to become very small; comparable to computer accuracy tolerances. Hence a nondimensional representation with larger numbers has greater accuracy. The state space representation in

non-dimensional form is:

$$\begin{bmatrix} \dot{q} \\ \ddot{q} \\ \dot{q}_p \\ \ddot{q}_p \end{bmatrix} = \begin{bmatrix} 0 & 1 & 0 & 0 \\ -\frac{k_{cz}}{m_c\omega_{cz}^2} & -\frac{b_{cz}}{m_c\omega_{cz}} & \frac{\rho A_c k_p}{m_c m_p \omega_{cz}^2}\int_0^L \Phi\, dl_c & \frac{\int_0^L \Phi\, dl_c}{m_c\omega_{cz}}\left(\rho A_c \frac{c_p}{m_p} - b_{cz}\right) - \frac{\Phi b_s}{m_c\omega_{cz}} \\ 0 & 0 & 0 & 1 \\ 0 & 0 & -\frac{k_p}{m_p\omega_{cz}^2} & -\frac{c_p}{m_p\omega_{cz}} \end{bmatrix} \begin{bmatrix} q \\ \dot{q} \\ q_p \\ \dot{q}_p \end{bmatrix}$$
$$+ \begin{bmatrix} 0 & 0 & 0 & 0 \\ -\frac{\rho A_c k_p v}{m_c m_p \omega_{cz}^2 D_m}\int_0^L \Phi\, dl_c & -\frac{\Phi \pi w R}{m_c \omega_{cz}^2 D_m} & \frac{\rho A_c}{m_c}\int_0^L \Phi\, dl_c & -\frac{b_{cz}}{m_c\omega_{cz}}\int_0^L \Phi\, dl_c - \frac{\Phi b_s}{m_c\omega_{cz}} \\ 0 & 0 & 0 & 0 \\ \frac{K_{pv}}{m_p\omega_{cz}^2 D_m} & 0 & 0 & 0 \end{bmatrix} \begin{bmatrix} \bar{V}_{zp} \\ \bar{F}_n \\ \ddot{Z}_s \\ \dot{Z}_s \end{bmatrix} \tag{2.35}$$

$$q = \begin{bmatrix} 1 & 0 & 0 & 0 \end{bmatrix} \begin{bmatrix} q \\ \dot{q} \\ q_p \\ \dot{q}_p \end{bmatrix} \tag{2.36}$$

2.5 Implementation Issues

As stated in Chapter 1, the vertical AFM dynamics in the equations above will be implemented as Simulink models. The current form results in a simulation that captures the full transient and steady state response. Because tapping mode simulations have a constant shaker amplitude and frequency, shaker transients can be replaced with the shaker steady state response. This step also vastly improves the simulation speed. In order to do this, the steady state solution must be analytically found. The AFM cantilever equation of motion can be rewritten as,

$$m_c\omega_{cz}\ddot{q} + b_{cz}\omega_{cz}\dot{q} + k_{cz}q = A_1 q_p + A_2\dot{q}_p + A_3\bar{V}_{zp} + A_4\bar{F}_n + A_5\ddot{Z}_s + A_6\dot{Z}_s \tag{2.37}$$

The steady solution of the differential equation above is the superposition of the six forcing terms.

$$q(\tau_n) = q_1(\tau_n) + q_2(\tau_n) + q_3(\tau_n) + q_4(\tau_n) + q_5(\tau_n) + q_6(\tau_n) \tag{2.38}$$

The shaker displacement is then defined as,

$$Z_s(\tau_n) = \frac{z_s}{D_m} \sin\left(\frac{\omega_d}{\omega_{cz}}\tau_n\right) \tag{2.39}$$

The shaker velocity is found by differenting the previous equation,

$$\dot{Z}_s(\tau_n) = \frac{z_s\omega_d}{D_m\omega_{cz}} \cos\left(\frac{\omega_d}{\omega_{cz}}\tau_n\right) \tag{2.40}$$

Similarly, the shaker acceleration is,

$$\ddot{Z}_s(\tau_n) = -\frac{z_s\omega_d^2}{D_m\omega_{cz}^2} \sin\left(\frac{\omega_d}{\omega_{cz}}\tau_n\right) \tag{2.41}$$

These equations can be used as forcing inputs in solving for the steady state response. The steady state response due to the shaker acceleration becomes,

$$q_5(\tau_n) = -\frac{A_5 z_s\omega_d^2}{ZD_m\omega_{cz}^2} \sin\left(\frac{\omega_d}{\omega_{cz}}\tau_n + \phi_s\right) \tag{2.42}$$

The coefficient A_5 is given by,

$$A_5 = \rho A_c\omega_{cz}^2 \int_o^L \Phi dl_c \tag{2.43}$$

Z is given by,

$$Z = \sqrt{(k_{cz} - m_c\omega_d^2)^2 + (b_{cz}\omega_d)^2} \tag{2.44}$$

and ϕ_s represents the system phase angle,

$$\phi_s = \tan^{-1}\left(\frac{b_{cz}\omega_d}{k_{cz} - m_c\omega_d^2}\right) \tag{2.45}$$

The response due the shaker velocity is found in a similar fashion,

$$q_6(\tau_n) = \frac{A_6 z_s\omega_d}{ZD_m\omega_{cz}} \cos\left(\frac{\omega_d}{\omega_{cz}}\tau_n + \phi_s\right) \tag{2.46}$$

where A_6 is given by,

$$A_6 = -b_{cz}\omega_{cz} \int_0^L \Phi dl_c - b_s\omega_{cz}\Phi(L) \tag{2.47}$$

Once the steady state responses have been found, they need to be inserted back into model's state vector. This of course requires the steady state velocity responses as well. The velocity

response due to the shaker acceleration is found by differentiating Equation (2.42).

$$\dot{q}_5(\tau_n) = -\frac{A_5 z_s \omega_d^3}{Z D_m \omega_{cz}^3} \cos\left(\frac{\omega_d}{\omega_{cz}}\tau_n + \phi_s\right) \tag{2.48}$$

The velocity response due to the shaker velocity is found similarly:

$$\dot{q}_6(\tau_n) = -\frac{A_6 z_s \omega_d^2}{Z D_m \omega_{cz}^2} \sin\left(\frac{\omega_d}{\omega_{cz}}\tau_n + \phi_s\right) \tag{2.49}$$

2.6 Differentiation Between Tapping Mode and Contact Mode

The dynamics stated in Section 2.4 apply to the AFM functioning in both tapping and contact mode. As the piezoelectric tube creates a constant lateral velocity, the bimorph shaker vertically excites the cantilever near its natural frequency. The Atomic Force Microscope responds to the surface profile by measuring the tip displacement and calculating the root mean square tip amplitude. The error between the actual RMS tip amplitude and the desired tip amplitude is fed to a PID controller which in turn vertically actuates the piezoelectric tube. Figure 2-2 shows a schematic of the control loop. Unlike in tapping

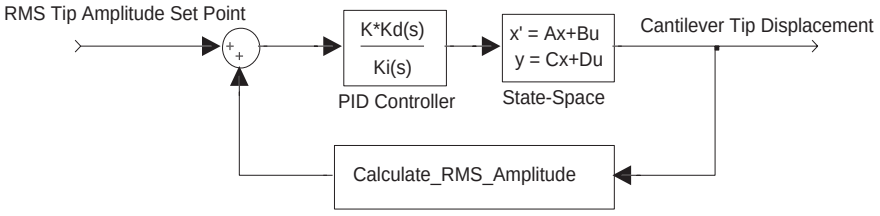

Figure 2-2: A Block Diagram of the AFM in Tapping Mode

mode, the bimorph shaker does not excite the AFM cantilever in contact mode. Hence, the only difference between tapping mode dynamics and contact mode dynamics is the removal of the third and fourth excitation terms from the u matrix in Equation (2.35). The piezoelectric tube creates a constant lateral velocity and the cantilever deflection responds in proportion to its stiffness. The error between the actual cantilever tip position and the desired deflection is sent to a PID controller which in turn actuates the vertical motion of the piezoelectric tube. Figure 2-3 shows a schematic of AFM operation in contact mode.

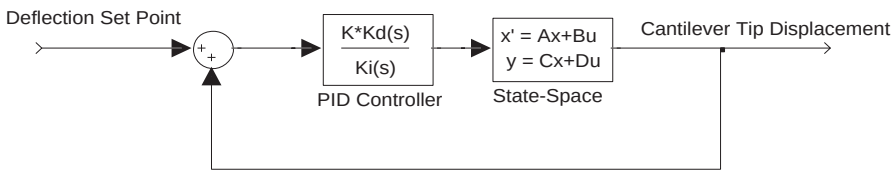

Figure 2-3: A Block Diagram of the AFM in Contact Mode

Chapter 3

A Review of Current Nanoscale Lateral Surface Force Models

In Chapter 2, the vertical dynamics of the AFM were described. This chapter will seek to build upon this foundation by explaining the normal force on the cantilever introduced earlier. Additionally, it will then show how nanoscale friction is more complex than in the macroscale. New models describing these forces and their relationships will be introduced and developed.

3.1 The Friction Problem

When an object is pushed across a surface, it feels a dissipative force opposite to the direction of motion called friction. Basic physics establishes dry friction to be proportional to the normal force on a body.

$$F_f = \mu F_n \tag{3.1}$$

The proportionality constant, known as the coefficient of friction, varies for varying pairs of materials. Additionally, the coefficient of friction is differentiated for static and kinetic conditions. There is no method to calculate the coefficient of friction *a priori*. Instead engineers rely on an extensive set of experimental results. However, this is only a suitable solution for macroscale problems.

The notion of *Normal Force* is very different at the nanoscale. Macroscale problems often have one dominating force like gravity that allow a simple calculation of the normal force

through force balance. At the nanoscale, however, the force balance is more complicated because a conglomerate of applied, adhesional, electrostatic among other forces are involved in the force balance. This complicates the frictional force calculation. It is quite clear that a new friction model is needed to deal with problems that involve very small characteristic lengths.

3.2 A Physical Understanding Based on Continuum Mechanics

When an object of any size and shape contacts a planar surface, that object deforms such that it has a real area of contact. This area differs from the apparent area of contact. For example, in the case of a spherical ball in contact with the ground, the apparent area of contact is infinitesimal. (The intersection of a sphere and a plane is a single point.) In reality, however, the ball elastically deforms to create a circular area of contact that distributes the forces on the ball to a pressure. Figure 3-1 shows an elastic sphere in contact with a planar surface. The nature of the deformation depends on the material properties, the geometry and the applied forces. Such an interaction is described in Hertz Contact Theory [9].

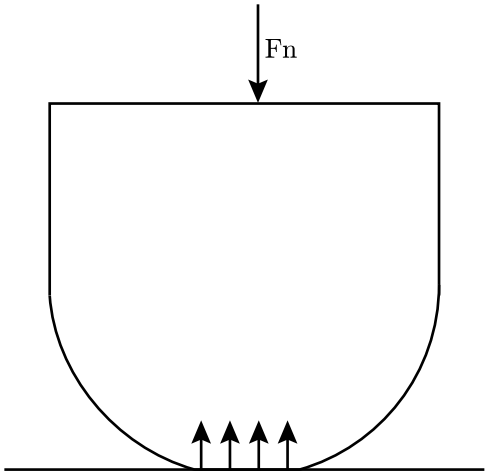

Figure 3-1: A Spherical Ball Under Elastic Deformation

Friction at the micro and the nanoscale, can be viewed as the tangential analogy to the description above. An applied force in the tangential direction will create an interfacial shear stress on the object. For relatively small forces, the frictional shear stress is elastic.

Small displacements due to the tangential force disappear upon its removal. As greater forces are applied, the frictional shear stress increases, but eventually can not maintain the strength of the contact. At a critical force, the friction reaches a maximum and the object transitions from small scale elastic movement to large scale sliding. The force-displacement curve is shown in Figure 3-2.

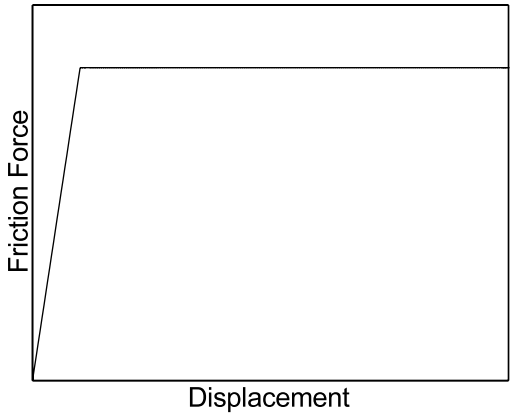

Figure 3-2: A Typical Friction-Force Displacement Curve

3.3 Bowden-Tabor Friction Models

Many nanoscale friction models rely on the Bowden-Tabor Friction Model proposed earlier in the century. It asserts that the force of limiting friction is proportional to the real area of frictional contact [10].

$$F_f = \tau_e A_f \tag{3.2}$$

The proportionality constant τ_e is the effective interfacial shear strength which is given by [11],

$$\tau_e = 2\left(\frac{1}{\tau_a} + \frac{1}{\tau_s}\right)^{-1} \tag{3.3}$$

To determine the real area of contact, Bowden and Tabor used Hertzian Contact Theory. The geometry of the AFM can be modeled as a spherical asperity on a planar surface. The

Hertzian result gives the radius of area of contact as [9],

$$a = \left(\frac{3F_n R_a}{4E}\right)^{1/3} \tag{3.4}$$

E, the effective interfacial Young's Modulus, is given by the following,

$$E = \left(\frac{1-\nu_a^2}{E_a} + \frac{1-\nu_s^2}{E_s}\right)^{-1} \tag{3.5}$$

Adhesion and surfaces are neglected in Hertzian Contact Theory. As length scales decrease into the nanometer range, forces due to adhesion become increasingly significant [12]. Hertz Contact Theory becomes no longer sufficient in providing an accurate area of contact for the Bowden-Tabor Friction Model.

Prior to finding a model that incorporates adhesion in its area calculation, it is important to understand the physical behavior of adhesion. Adhesion dramatically affects the normal forces on the asperity. As the asperity approaches the surface, it first experiences a tensile, *attractive*, force. Upon contact, elastic contact dominates, and the force on the asperity becomes compressive. As the asperity is pulled from the surface, adhesion continues to pull the asperity to the surface [13]. Adhesion, therefore, does not depend on the applied force. Instead, the effect is a nonlinear function of the height over the surface. Figure 3-3 shows a graph of the elastic and adhesional normal force as a function of height over the surface.

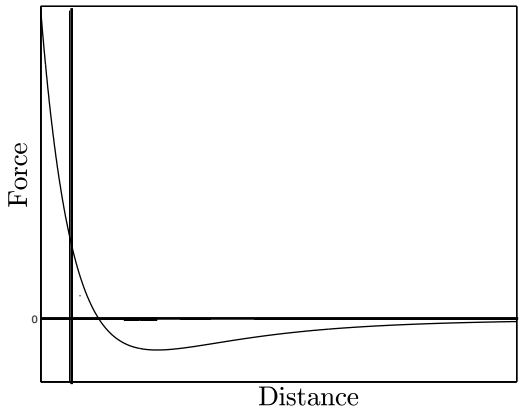

Figure 3-3: Normal Force Due to Elastic Contact and Adhesion as a Function of Distance

3.3.1 Johnson-Kendall-Roberts Area Calculation

The Johnson-Kendall-Roberts (JKR) Contact Theory is a continuum model of the physics of elastic adhesive contacts [14]. The theory incorporates adhesion to provide an improved calculation of the real area of contact. For a parabolic asperity, JKR theory gives the real area of contact to be [13]

$$A_f = \pi \left[\frac{3R_a}{4E} \left(F_n + 3\pi R_a \gamma + \sqrt{6\pi R_a \gamma F_n + (3\pi R_a \gamma)^2} \right) \right]^{2/3} \tag{3.6}$$

The difference between a spherical and a parabolic asperity in real area of contact is negligible [15]. Burns, Houston, Carpick and Mechalske use a near field scanning optical microscope to measure friction. The instrument provides an advantage over the AFM by decoupling the normal and friction force while maintaining nanometer length scales, and an asperity on planar surface geometry. They report an excellent agreement between experimental friction measurements and a JKR based Bowden-Tabor friction calculation.

3.3.2 Maugis-Dugdale Area Calculation

The Maugis-Dugdale (MD) theory describes contacts in which adhesional and elastic contact forces are comparable [16]. A dimensionless parameter ϕ governs the transition from a purely dry elastic Hertzian contact to one in which adhesion dominates in a JKR type contact.

$$\phi = \left(\frac{4R_a \gamma^2}{E^2 z_o^3} \right)^{1/3} \tag{3.7}$$

JKR theory is most applicable when $\phi > 5$ and adhesion dominates the asperity to surface interaction. Hertzian theory provides the best model when $\phi < 0.1$ and dry elastic contact is most significant. The Maugis-Dugdale theory provides an intermediate theory for when $\phi \sim 1$. The model converges to Hertzian Contact Theory as adhesion energy approaches zero and converges to the JKR model as it exceeds the elastic contact energy. Lantz, O'Shea, and Welland argue that the MD theory is most appropriate for an AFM with a sharp tip [12].

The Maugis-Dugdale theory can be summarized as an effort to accurately find the area of elastic contact and the area of adhesional interaction. Figure 3-4 shows the radius of elastic contact, a, and the radius of adhesional interactions c. The two radii can be found

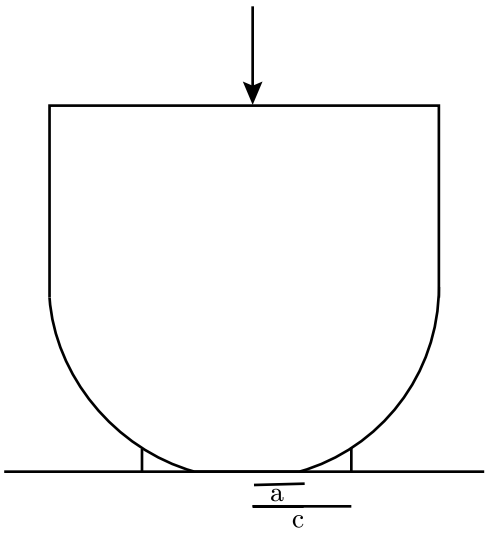

Figure 3-4: A Maugis-Dugdale Type Contact: Elastic Contact and Adhesion

by simultaneously solving Equations (3.8) and (3.9) [12].

$$\frac{\lambda\bar{a}^2}{2}\left[(\eta^2-2)\cos^{-1}(1/\eta)+\sqrt{\eta^2-1}\right]+\frac{4\lambda^2\bar{a}}{3}\left[\sqrt{\eta^2-2}\cos^{-1}(1/\eta)-\eta+1\right]=1 \tag{3.8}$$

$$\bar{P_a}+\bar{P_c}=\bar{a}^3-\lambda\bar{a}^2\left[\sqrt{\eta^2-1}+\eta^2\cos^{-1}(1/\eta)\right] \tag{3.9}$$

η is the ratio of c to a. The force due to elastic contact, P_a, and the force due to adhesion, P_c, are given by [12],

$$P_a=\frac{4Ea^3}{3R_a} \qquad P_c=-2\sigma_o[c^2\cos^{-1}(1/\eta)+a\sqrt{c^2-a^2}] \tag{3.10}$$

$\bar{a}$, $\bar{c}$, $\bar{P}$ and λ are non-dimensional parameters defined as [12]:

$$\begin{array}{lllll} \bar{a} & = & a\left(\frac{4E}{6\pi\gamma R_a^2}\right)^{1/3} & \bar{c} & = & c\left(\frac{4E}{6\pi\gamma R_a^2}\right)^{1/3} \\ \bar{P_{a,c}} & = & \frac{P_{a,c}}{2\pi\gamma R_a} & \lambda & = & 2\sigma_o\left(\frac{9R_a}{32\pi\gamma E^2}\right) \end{array} \tag{3.11}$$

With two different interfacial radii, it becomes difficult which one should be used in the Bowden-Tabor Friction Model. Experimental results suggest an intermediate effective radius b, governed by a numerical weighting factor p.

$$b=c+p(c-a) \tag{3.12}$$

Empirical results show that p is approximately equal to 0.4. The Bowden-Tabor Friction is then given by:

$$F_f = \tau \pi b^2 \tag{3.13}$$

3.3.3 Tip-Surface Contact Stiffness

The Bowden-Tabor model when used with Hertz, JKR, or MD Contact Theory provides a good description of sliding friction. Because most tangentially applied forces are great enough to initiate large scale sliding, the Bowden-Tabor model alone suffices in describing the friction force. In some cases, only small tangential forces are applied and the frictional force does not reach its upper limit. In these cases, friction is a type of elastic deformation in shear. The friction force is [12]:

$$F_f = 2\tau b^2 \left[\cos^{-1} \left(\sqrt{1 - \left(\frac{2Gx}{\tau b} \right)^2} \right) + \left(\frac{2Gx}{\tau b} \right) \left(1 - \left(\frac{2Gx}{\tau b} \right)^2 \right) \right] \tag{3.14}$$

where G, the interfacial shear modulus, is given by,

$$G = \left(\frac{2 - \nu_1}{G_a} + \frac{2 - \nu_2}{G_s} \right)^{-1} \tag{3.15}$$

Equation (3.14) is commonly simplified by assuming: (1) there is no slip at the periphery of the contact area, (2) there is no coupling between normal force and friction. The simplified friction force becomes [12],

$$F_f = 8bGx \tag{3.16}$$

3.3.4 Limitations of the Bowden-Tabor Friction Model

Despite a sound foundation in continuum mechanics, the Bowden-Tabor friction model has its limitations in predicting the friction force in an AFM scan. The primary difficulty is that it is unclear whether a continuum mechanics model applies in the single nanometer range. A 4 nm radius of contact area corresponds to about 100 atoms. With so few atoms, the average effect of bulk properties like shear strength, Young's modulus, shear Modulus may no longer be as statistically valid [17]. With 100 atoms, the variations in bulk properties due to grain size are important as well. Additionally at that scale, it is unlikely that the effective values of the bulk properties would be the same as their macroscale counterparts.

The Bowden-Tabor friction model would require experimental values for the bulk properties for every combination of sample and asperity materials. Moreover, it is unlikely that these effective values would be accurately measured.

The need for effective values of bulk properties brings about another difficulty. Section 3.2 introduced the need to model friction so that it is known *a priori*. While bulk properties are assumed as fundamental in the macroscale, they can not be viewed as such in the nanoscale when they are continually being measured. Additionally, the Maugis- Dugdale model requires p as an experimental tuning factor. This is because the model does not capture the true physical nature of the friction. For example, the dimensionless number ϕ should not be needed as a selection factor of three distinct contact theories. The physical nature of a sliding asperity on a planar surface has not changed, and hence a single model capturing the true physical nature of nanoscale contact should suffice.

Lastly, the Bowden-Tabor Friction model is a static model. It does not include the dynamic nature of the AFM. It does not predict whether friction is the only type of surface interaction of there are others as well. Coupling between the motion of the cantilever tip and the friction force is also not explained. In the next sections, a new paradigm will be used to model the surface forces as they relate specifically to the AFM. An atomic view will be used to explore the physical nature of these forces and any dynamic coupling between the AFM and the surface.

3.4 A Physical Understanding Based on Potential Functions

Previously, the interaction between a planar surface and an approaching asperity was described as a combination of adhesion and elastic deformation. Alternatively, these interactions can be described on an atomic scale. At a sufficiently close distance, attractive van der Waals bonds form between the asperity and the surface. When an asperity approaches the surface, numerous increasingly attractive van der Waals bonds form [18]. See Figure 3-5. Van der Waals bonds are interatomic/molecular interactions that occur due to random variations in the electron density of non-polar molecule. While each bond is about ten percent as strong as a chemical bond, the cumulative attractive potential of the van der Waals bonds over a nanoscale area can be very significant [19]. These van der Waals bonds form the atomic basis of adhesion. For this reason, the effects of adhesion are more prominent

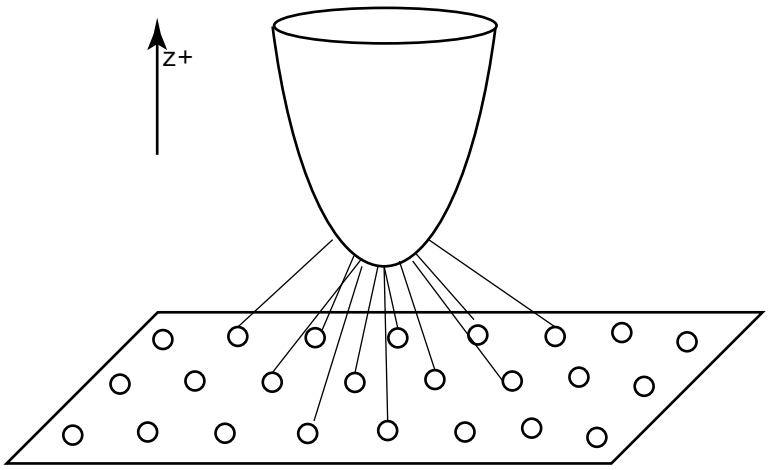

Figure 3-5: A van der Waals bond Friction Mechanism

at small length scales.

As the asperity approaches the sample surface further, a repulsive force dominates. This interaction comes from the electric repulsion of the respective electron clouds. The physical behavior of the van der Waals bonds and the electron cloud repulsion can be described by their energy. Late in the 19th century, Lennard and Jones captured these two universal phenomena in a single potential function [20],

$$V_z = 4\epsilon \left[\left(\frac{z_o}{z} \right)^{12} - \left(\frac{z_o}{z} \right)^{6} \right] \tag{3.17}$$

z_o and ϵ are Lennard-Jones parameters that must be experimentally measured for varying pairs of materials. Taking the negative directional derivative with respect to z gives the force between the two bodies as a function of their separation.

$$F_n = -\frac{\partial V_z}{\partial z} = 24\epsilon \left[2 \left(\frac{z_o^{12}}{z^{13}} \right) - \left(\frac{z_o^{6}}{z^{7}} \right) \right] \tag{3.18}$$

Appropriately, Equation (3.18) is the mathematical equivalent of Figure 3-3.

3.5 Potential Energy Based Models

It is important to pause before proceeding to make proper definitions. Friction force is a *dissapative* force that acts opposite to the direction of motion. In the macroscale, dry

friction is often described as the only horizontally accting force. In the nanoscale, this is not necessarily the case. Numerous surface interactions can combine to form a net horizontally actging force. This tangential force can be approximated by handling it in a method similar to the one used for the normal force. A potential function is obtained, and the net lateral force is its negative directional derivative with respect to the scanning direction. The use of a potential function without any additional energy transfer mechanisms, or dissipative forces implies a conservative force which by definition is different from friction. This does not exclude the existence of other lateral surface forces whch may be conservative and hence described by potential functions. Many potential functions of varying accuracy and complexity have been proposed to describe these surface forces. The following section summarizes some of them.

3.5.1 The Buldum-Ciraci Model

Buldum and Ciraci proposed a model for an asperity sliding on a planar surface. It accounts for a single atom in the asperity interacting with individual atoms in the surface. Figure 3-6 gives a good schematic of the rationale behind the model. Many interactions contribute

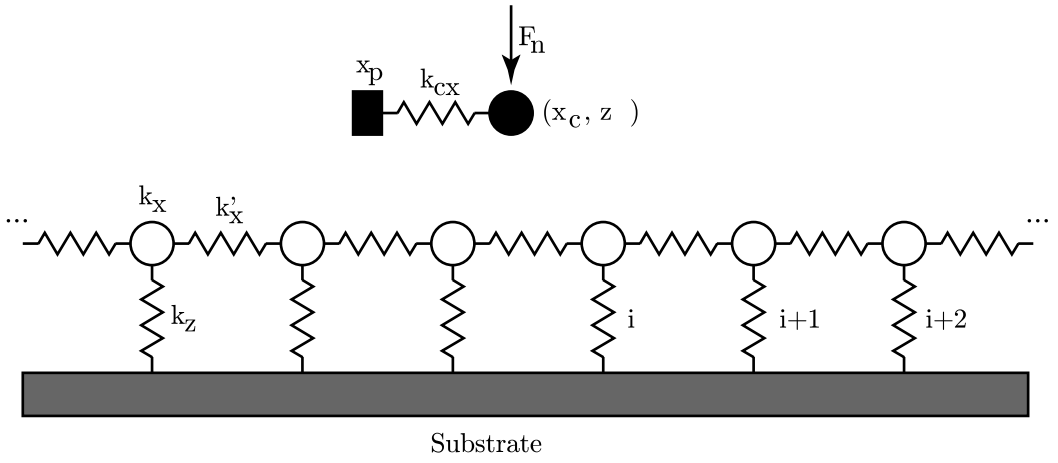

Figure 3-6: A Schematic of the Buldum-Ciraci Model

to the overall potential function. The asperity atom, through the cantilever, has an elastic potential to the rest of the AFM (k_{cx}). Additionally, each of the surface atoms have an elastic potential to each other. This potential includes stiffness due to vertical compression against the substrate (k_z), horizontal displacement relative to the substrate k_x, and

horizontal displacements relative to each other k'_x. Lastly, there is a potential between the asperity atom and every surface atom. Defining a coordinate vector $\vec{r}_c = (x_c, z)$, the total potential is then given by,

$$\begin{aligned} V_T &= \sum_i V_{xi}(|\vec{r}_c - \vec{r}_i|) + \frac{1}{2}k_{cx}(x_c - x_p)^2 + \sum_i \frac{1}{2}k_x(x_i - x_{i,0})^2 + F_n z \\ &\quad + \sum_i \frac{1}{2}k'_x[(x_{i+1} - x_{i+1,0}) - (x_i - x_{i,0})]^2 + \sum_i \frac{1}{2}k_z(z_i - z_{i,0})^2 \end{aligned} \tag{3.19}$$

The interaction potential between the asperity and individual atom is described by a Lennard-Jones Potential with ϵ=0.84eV and z_o=2.56 Å[1]. F_n accounts for the externally applied normal force. It is also given by

$$F_n = \sum_i \left[\frac{\partial V_{zi}}{\partial z}\right] = \sum_i k_z(z_i - z_{i,0}) \tag{3.20}$$

With the potential function described above, the equation of motion of the cantilever tip in the x direction becomes [21],

$$m\ddot{x}_c + \sum_i \frac{\partial V_{xi}}{\partial x_c} + F_n \frac{\partial z_c}{\partial x_c} + k_c(x_c - x_p) = 0 \tag{3.21}$$

The Buldum and Ciraci model thoroughly incorporates many of the pertinent energies. It derives the lateral surface force from an extensive set of energy summations. This results in a mathematical description that captures the qualitative nature of nanoscale surface interactions. It describes the stick-slip behavior sometimes observed in contact mode scans. It also predicts a force that is at times wearless and adiabatic. The model describes dissipation as an energy transfer from the asperity atom to the vibrational energy of the surface atoms. The vibration of atoms is the equivalent of heat energy that can not be recovered.

3.5.2 Gyalog-Thomas Model

Gyalog and Thomas proposed a simpler two dimensional surface interaction model for the Atomic Force Microscope. It still uses an energy potential to determine the surface force, but it does not account for the effects of the individual atoms of the surface. Instead, it

[1]In Section 3.4, the Lennard-Jones potential was described as the vertical distance away from a planar surface of atoms. It also equally describes the potential in a radial direction away from one or many atoms.

summarizes the saw-tooth behavior with a combination of sinusoids that act as Fourier series terms. The surface to asperity potential in the lateral directions is given as [22]:

$$V_{xy} = a_1 \left[\cos\left(\frac{2\pi}{\lambda_l} x_c\right) + \cos\left(\frac{2\pi}{\lambda_l} y_c\right) \right] + a_2 \cos\left(\frac{2\pi}{\lambda_l} x_c\right) \cos\left(\frac{2\pi}{\lambda_l} y_c\right) \tag{3.22}$$

As in the previous model, the horizontal surface force is given by the directional derivative with respect to the scanning direction.

$$\vec{F}_{xy} = -\frac{\partial V_{xy}}{\partial x_c}\hat{x} - \frac{\partial V_{xy}}{\partial y_c}\hat{y} \tag{3.23}$$

Because this thesis investigates surface forces in just one direction, the surface asperity potential is reduced for a one dimensional scan:

$$V_x = a_3 \cos\left(\frac{2\pi}{\lambda_l} x_c\right) + a_4 \tag{3.24}$$

Similarly, the tangential force becomes a pure sinusoid:

$$F_x = F^* \sin\left(\frac{2\pi}{\lambda_l} x_c\right) \tag{3.25}$$

The tip sample interaction alone does not describe the horizontal motion of the AFM cantilever. Its dynamic stability depends on the total energy of the system which in turn depends on the deformation of the cantilever. If the coordinate vectors are changed to include just horizontal direction, $\vec{r}_c = (x_c, y_c)$, then

$$V_T = V_{xy} + \frac{1}{2}(\vec{r}_c - \vec{r}_p)K(\vec{r}_c - \vec{r}_p) \tag{3.26}$$

The dynamics stability conditions are then defined as the following:

$$\frac{\partial V_T}{\partial x_c}\hat{x} + \frac{\partial V_T}{\partial y_c}\hat{y} = 0 \tag{3.27}$$

$$\psi_{1,2} \geq 0 \tag{3.28}$$

$\psi_{1,2}$ are the eigenvalues of the Hessian $\partial^2 V_T / \partial x_c \partial y_c$ [21].

Over the course of a typical AFM contact mode scan, the stability conditions are not always met. As a result the AFM shows a regular saw-tooth pattern of unstable irreversible

jumps. The model also describes the adiabatic nature of tangential surface forces. Gyalog and Thomas present evidence in which their model agrees with experimental AFM scans. The model also agrees with the Buldum and Ciraci model, but describes the phenomena more succinctly.

3.5.3 Johnson and Woodhouse Model

Johnson and Woodhouse proposed a one dimensional model very similar to that of Gyalog and Thomas. A potential function is still used to determine the surface force, a geometric constraint is added to predict the occurrence of the unstable slips of the cantilever, and the lateral dynamics of the AFM are included as well. The model is built upon a variety of sources confirming the sinusoidal nature of the lateral potential function. Zhong and Tomanek give the interaction potential based upon first principles calculations [23]. In another article, they, with Thomas, state that for a given normal force the interaction potential is [24],

$$V_x = V^* \cos\left(\frac{2\pi}{\lambda_l} s\right) \tag{3.29}$$

The tangential surface force is then found to agree with the one dimensional Gyalog and Thomas result found in Equation (3.25). A fine distinction is made, however. Johnson and Woodhouse state the tangential force depends on the slip distance, s, and not the cantilever position, x_c. The difference between the two displacements is caused by the lateral contact stiffness of the surface. The experimental results, however, do not show a lateral sinusoidal force. This is because it is coupled to the lateral motion of the AFM. To capture the coupling, Johnson and Woodhouse model the AFM lateral dynamics as a mass-spring-dashpot system. The equation of motion of the cantilever tip is,

$$m\ddot{x}_c + b_{cx}\dot{x}_c + k_{cx}x_c = F^* \sin\left(\frac{2\pi}{\lambda_l} s\right) \tag{3.30}$$

In addition to the dynamics of the AFM, the cantilever tip must follow the geometric constraint below [17],

$$s = x_p - x_c - x_s \tag{3.31}$$

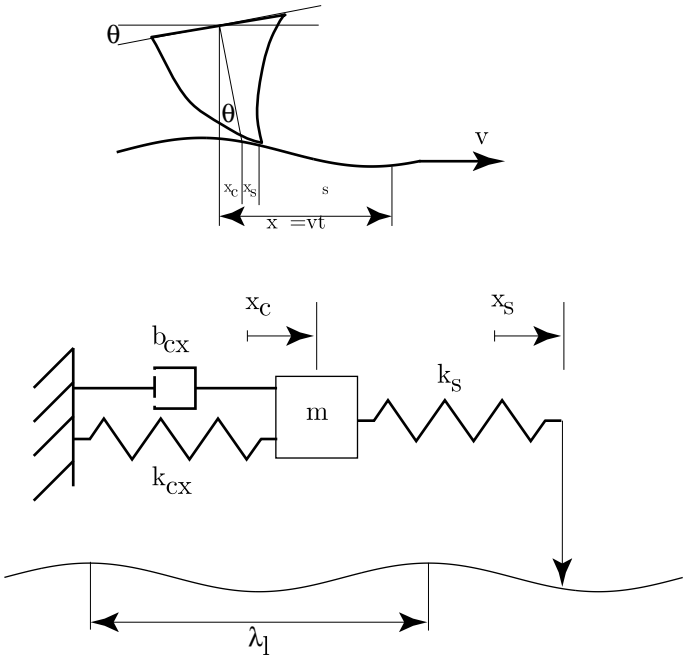

Figure 3-7: AFM Cantilever in Contact Mode

Johnson and Woodhouse introduce a non-dimensional notation.

$$\begin{array}{lllllll} S = s/\lambda_l & X_c = x_c/\lambda_l & X_s = x_s/\lambda_l \\ X_p = x_s/\lambda_l & F_c = F_x/F^* & \tau = \omega_{cx}t \\ K_c = \lambda_l k_{cx}/F^* & K_s = \lambda_l k_s/F^* & \zeta = b_{cx}\omega_{cx}/2k_{cx} \end{array} \tag{3.32}$$

Using the convention above Equations (3.30) and (3.31) are rewritten:

$$\sin(2\pi S) = K_c \left[\ddot{X}_c + 2\zeta\dot{X}_c + X_c\right] \tag{3.33}$$

$$S = X_p - X_c - (1/K_s)\sin(2\pi S) \tag{3.34}$$

Simultaneously solving Equations (3.33) and (3.34) gives a unique trace for the surface force in time trace. Figure 3-8 gives a typical result of the model. Under stable conditions, the force follows a sinusoid rotated about the origin. As with other models, this force is completely conservative. Periodicly, however, the cantilever becomes unstable and snaps from a high to a low a friction force. These unstable slips are irreversible and also cause damped oscillation of the cantilever as it continues back on its stable path. By coupling

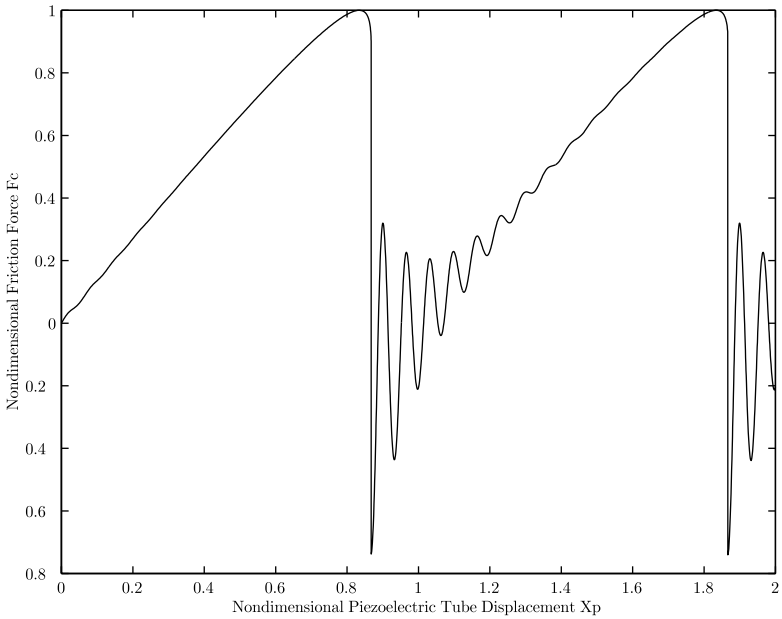

Figure 3-8: Illustrative Example of Johnson-Woodhouse Model

the AFM dynamics to the force derived from the interaction potential, the model is able to capture the salient features of the experimental results. It shows both the adiabatic nature of the net surface force as well as the saw-tooth shape variations.

3.6 Other Atomic Friction Models

While it is clear that the models based on the interfacial potential capture many of the features of the experimental results it is not clear whether some of interfacial interactions are neglected. In particular, the models above neglect any dependence on the cantilever velocity.

3.6.1 Velocity Dependant Models

Three sources of velocity dependent friction have been proposed. The first friction source is due to electromagnetic variations between the AFM cantilever tip and the surface. The second is due to an exchange of electrons between the two bodies. The last is due to the exchange of phonons. All of these models are derived directly from first principles and yield friction values on the order of picoNewtons [18]. Experimental results show the

friction measurements are on the order of nanoNewtons. These velocity dependant models, therefore, describe insignificant parts of the surface to asperity interaction.

3.6.2 Other Models

The models above give a good description of the current state of the literature on the lateral surface force in the AFM: interactions for a single asperity on a planar surface. This, however, is only a subset of the literature on nanoscale interactions. Much attention has been given to filmed or quasi-dry surfaces. In addition, models have been proposed that include multiple asperities in contact with a surface. The state and rate dependant model describes friction for a multiple contact interface [25]. Dynamic friction models that cover a wide variety of length scales have also been proposed [26]. It is unlikely, however, that such models will elucidate the nature of surface interactions as they apply directly to the AFM.

Chapter 4

Expansion of Johnson-Woodhouse Model to Tapping Mode

Chapter 3 explained the physical nature of normal, lateral surface and frictional forces using three paradigms: continuum mechanics, atomic potential functions and first principles. It also described a variety of contact mode lateral surface force models. One model proposed by Johnson and Woodhouse seemed particularly promising for further theoretical work. This chapter will build upon this foundation by expanding the Johnson-Woodhouse contact model to tapping mode.

4.1 Rationale for Selection of Johnson-Woodhouse Contact Mode Model

Of all the models described in Chapter 3, the Johnson-Woodhouse Contact Mode Model was most suitable for further analysis. It had many attractive features. First, its sinusoidal interaction potential is agreed upon by many sources including ones with first principles type derivations. Second, the model agrees with a vast portion of the experimental results. It shows the stick-slip nature of nanoscale surface forces and predicts a force that can be conservative. Lastly, the model captures the dependence of this force on the AFM properties. Many models had these features, but none were as well developed. It included a complete description of the horizontal dynamics of the AFM and the role that the surface interactions play in it. Lastly, key equations and parameter values were stated such that

the model lent itself to reproduction and implementation.

4.2 Development of Tapping Mode Model

The expansion of a contact mode model lies on one assertion: the form of the surface interaction potential is the same for both modes of AFM operation. The potential functions proposed depend on material properties and geometry of the sample and the probe. The physical situation of an asperity moving above a planar surface is the same, and therefore the potential function must be the same.

Equation (3.17) states the Lennard-Jones potential as a function of height. In the meantime, Equation (3.25) summarizes the contact mode models with a potential function that is sinusoidally dependent on lateral displacement. A tapping mode lateral surface force model based on potential functions requires a dependence on not just one but both directions. The difficulty becomes combining the two potentials such that the equations remain true.

A second assumption is made: the only way that the lateral position affects the interaction potential is in the sinusoidal manner described earlier. The only other way to affect the potential function is by making V^* dependant on horizontal position, and this would lead to a non-sinusoidal friction force which is contrary to experimental behavior. Because V^* is not a function of lateral position then it must be a function of vertical position.

$$V_{xz} = V_z^* \cos\left(\frac{2\pi s}{\lambda_l}\right) \tag{4.1}$$

It is reasonable to equate V^* to $V(z)$ found by the Lennard Jones potential. This leaves an intuitive result. The interaction potential continues to vary at the lattice spacing, while the magnitude of the variation is dependant upon the height above the surface.

$$V_{xz} = 4\epsilon\left[\left(\frac{z_o}{z}\right)^{12} - \left(\frac{z_o}{z}\right)^{6}\right]\cos\left(\frac{2\pi s}{\lambda_l}\right) \tag{4.2}$$

Once the interaction potential is known, taking the negative derivative with respect to the horizontal direction gives the friction force:

$$F_x = -\frac{\partial V_{xz}}{\partial s} = 4\epsilon\frac{2\pi}{\lambda_l}\left[\left(\frac{z_o}{z}\right)^{12} - \left(\frac{z_o}{z}\right)^{6}\right]\sin\left(\frac{2\pi s}{\lambda_l}\right) \tag{4.3}$$

The maximum lateral force F^* for a given vertical position becomes:

$$F^* = 4\epsilon \frac{2\pi}{\lambda_l} \left[\left(\frac{z_o}{z} \right)^{12} - \left(\frac{z_o}{z} \right)^{6} \right] \tag{4.4}$$

4.3 Implementation

As with the AFM model, the lateral dynamics model requires some preparatory steps to ease the simulation process. As written the current model has no way of interfacing with the AFM dynamics model. It takes a Lennard-Jones distance as an input. This type of distance is very different from the vertical probe sample deformation defined in the AFM model. For example, the AFM model can describe a contact mode with a zero deformation. A zero Lennard-Jones distance means the nuclei of two atoms are in the same place. This non-physical result causes an infinite potential and force. Instead, the Lennard Jones distance is on the order of angstroms. To solve this discrepancy in distances, the normal force from the AFM model, and not the vertical position is used as an output. The Lennard-Jones force function found in Equation (3.18) is then solved for the corresponding distance[1]. In this way, the two dynamic models are interfaced with each other.

Using the Lennard Jones potential and force functions to interface the vertical dynamics and friction models causes further implementation issues. First, it requires that the functions be fairly accurate. In order to assure this, two steps were taken. First, it was assumed that the equilibrium distance between two atoms of 2.56 Åwould be similar for an asperity on a planar surface. Intuitively, electron clouds should cause repulsion at a similar distance, and hence the other interatomic forces should apply at similar distances. Once the equilibrium distance was found, Equation (3.18) was differentiated to find the distance at which the minima occurs. The function was evaluated at that distance to give the minimum force. The ϵ energy parameter was then tuned such that the minimum Lennard Jones force was equated to a minimum normal force found from a Maugis-Dugdale calculation in a tapping mode simulation.

Repeatedly solving with fine resolution the Lennard-Jones force function using numerical methods requires some care. First, the normal force step size needs to be fairly small. This is ensured by tightening the tolerance on the differential equation solver. This step improves

[1]The Maugis-Dugdale model used to calculate normal force in the AFM model very closely approximates the Lennard-Jones Force. It is therefore reasonable to equate the two forces.

convergence of the root finding algorithm. The next step improves the accuracy of the algorithm. As written, the function raises a number on the order of angstroms to the negative thirteenth power! This severely test the Matlab/machine tolerance. Instead of its current form Equation (3.18) can be rewritten as,

$$F_n z_o = 24\epsilon \left[2U^{13} - U^7\right] \tag{4.5}$$

using the change of variable: $U = z_o/z$. In this way, calculations can remain much greater than machine tolerances.

The last issue of implementation has to do with the time input of the lateral dynamics model. In contact mode, the AFM model time is the same as the lateral dynamics model time. This is because the cantilever tip is always in contact with the surface. This is not the case in tapping mode. Instead special care has to be taken to only input the times in which the tip has touched down. Once the contact times are found, the lateral dynamics model can calculate the relative displacement, and surface forces when in contact.

Chapter 5

Simulink Lateral Surface Force Simulations

Chapter 2 developed a model of the AFM dynamics in the vertical direction. Chapter 3 found an appropriate surface force model for the AFM in contact mode, and Chapter 4 expanded it to tapping mode. This chapter will attempt to put all of this together into a single simulation based upon the AFM operation parameters. First, the Simulink models for both contact and tapping modes will be qualitatively explained. Second typical traces in both modes of operation will be presented. Lastly, conclusions will be made about the relative magnitude of friction in the two modes.

5.1 Contact Mode Simulink Model

5.1.1 AFM Vertical Dynamics Model

The vertical dynamics of the AFM makes up the first portion of the contact mode Simulink model. The block diagram shown in Figure 5-1 is built upon a Simulink tapping mode simulation [27]. The piezoelectric tube-cantilever model block encompasses the state space representation found in Equation (2.35). The shaker inputs are removed so that only the first two terms of the input vector are used. The system calculates the absolute vertical tip position for the 'computecontact' function[1] which uses the Maugis Dugdale model to calculate normal force among other physical quantities [27]. The absolute cantilever deflection is

[1]The Matlab Code for the function is in Appendix C.3.

then subtracted from the setpoint to create an error signal sent to the controller. Figure 5-2 shows that the controller is composed of just a PID controller and the initial piezoelectric tube command voltage.

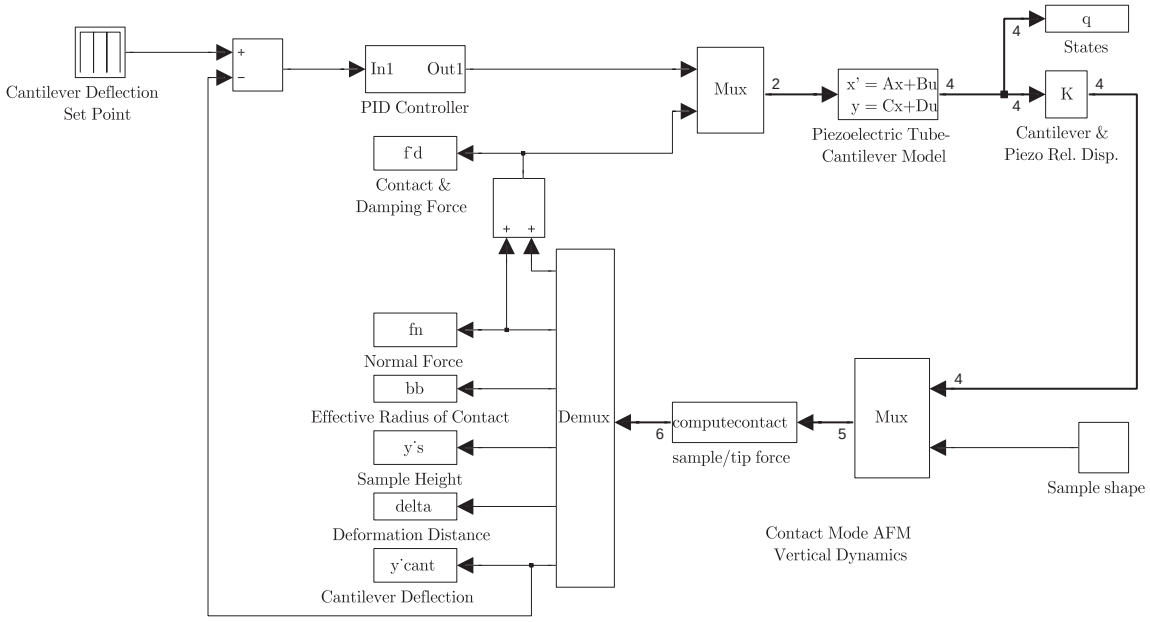

Figure 5-1: A Block Diagram of the Atomic Force Microscope Model

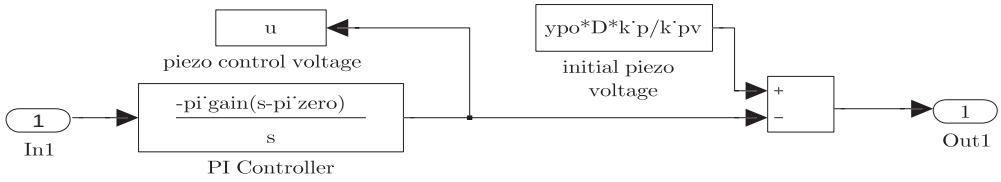

Figure 5-2: A Schematic of the Contact Mode PID Controller

The model above has many useful features. It allows the user to control the cantilever deflection set point. It also allows for scans of varying sample shapes. It also captures transients of the cantilever and piezoelectric tube due to variations in the sample surface. For the purposes of this investigation, each of the contact mode simulations will have the

same parameter values except one: the cantilever deflection set point. An atomically flat surface will be scanned each time. The simulation will begin at a height of 300 nanometers above the surface and will run until the cantilever deflection setpoint is reached. At that point, the lateral dynamics model simulates the lateral surface force.

5.1.2 Friction Model

Because the normal force is constant for contact mode scans of atomically flat surfaces, the simulation procedure is greatly simplified. The Lennard Jones distance need only be calculated once after the steady state cantilever deflection is reached. The AFM lateral dynamics model can therefore be decoupled from the AFM vertical dynamics model.

The tangential force portion of the Simulink model simply implements Equations (3.33) and (3.34). Figure 5-3 shows its block diagram. The centrally located block conveys the

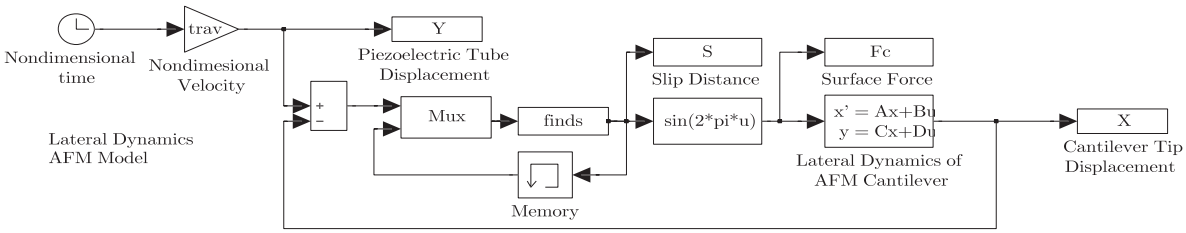

Figure 5-3: A Block Diagram of the Contact Mode Friction Model

sinusoidal dependence of the surface force on slip distance. It acts as the input to the state space representation of the lateral dynamics of the AFM cantilever. The nondimensional time is multiplied by the nondimensional scan velocity, trav, to give the piezoelectric tube position. The cantilever position in combination with the piezoelectric tube position is then used as the input to the 'finds'[2] function which uses a numeral root finding algorithm to output the slip distance. The memory block aids in its functionality by using the output as the new guess for the solution.

The model operates such that a scanning velocity of the piezoelectric tube laterally stretches the cantilever. In other words, the piezoelectric tube pulls the cantilever behind it. This causes the cantilever displacement, x_c, to be positive for a positive surface force and

[2]The Matlab Code for the function is in Appendix C.5

vice versa. These features will become particularly important in analyzing the simulation results.

5.2 Contact Mode Simulation Procedure

The simulation is run by executing a fully automated Matlab script that runs Simulink models, changes the cantilever deflection, and saves pertinent results[3]. It first executes a parameter file that initializes the model[4]. The values of the parameters are summarized in Appendix B. The script then calls the AFM vertical dynamics model. Because the state space equations describe a fourth order linear differential equation without discontinuities, Matlab's 'ode45' differential equation solver is sufficient for achieving a converging solution. The default tolerances are used because of the nondimensional nature of the model. The Matlab script then executes the second parameter file which initializes the friction Simulink model[5]. The file finds the Lennard-Jones distance from the steady state normal force. The remaining friction model parameters are initialized. The script then calls the friction model. Because the friction model is a nonlinear second order differential equation with discontinuities, Matlab's 'ode23s' differential equation solver is used. As before, the default tolerances are used and the simulation is run for $2/trav$ nondimensional time units. In this way, it is ensured that the simulation runs for two full sinusoid periods.

5.3 Contact Mode Simulation Results

The lateral surface force can be found for a variety of operating conditions using the Simulink models described above. The model states that the friction force depends on two parameters: the nondimensional cantilever and contact stiffnesses. The value of K_c is varied by changing the cantilever deflection set point or in other words by changing the normal force. Five simulations were run at five different cantilever deflection set points. Table 5.1 shows the deflection, normal force, and nondimensional stiffnesses for each of the five simulations. Contact stiffnesses, in actuality, depend upon Equation (3.16). Effective nanoscale shear moduli values are not easily attainable. Instead, the contact stiffness was estimated as

[3]The Matlab code for this script is found in Appendix C.1.
[4]The Matlab code for this parameter file is found in Appendix C.2.
[5]The Matlab code for the parameter file is included in Appendix C.4.

having a value three fourths that of the cantilever stiffness. Figure 5-4 shows the tangential

Number	Deflection (nm)	Normal Force (μN)	Cantilver Stiffness	Contact Stiffness
1	100	1.9838	39.432	29.574
2	250	4.9589	14.900	11.753
3	500	9.9183	7.4186	5.5640
4	750	14.877	4.9797	3.7348
5	1000	19.836	3.7643	2.8232

Table 5.1: Parameters for Contact Mode Surface Force Simulations

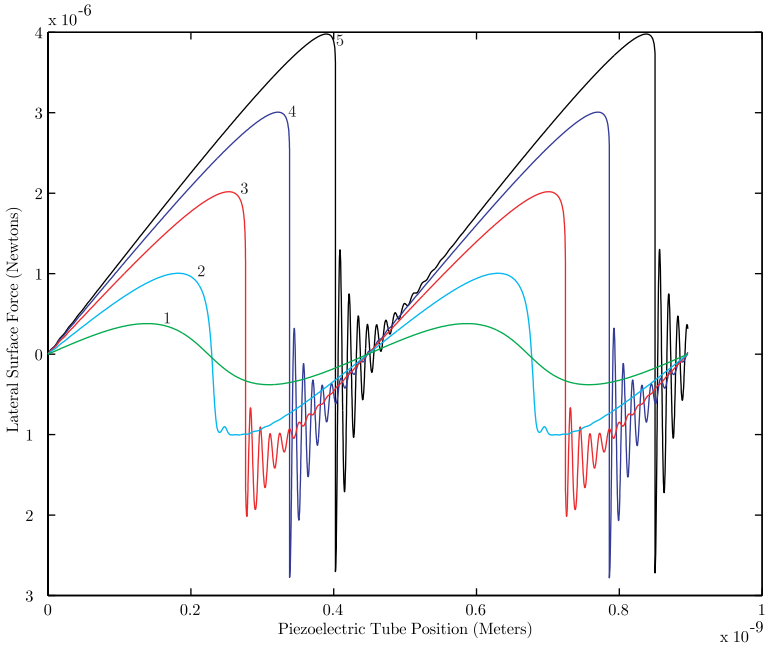

Figure 5-4: Results of Surface Force Simulations for Five Cantilever Deflections

force results for five different cantilever deflection set points[6]. Trace 1 shows the case of a small normal force. Slip distance is nearly identical to piezoelectric tube position and hence the trace shows the sinusoidal dependence of the surface force on the piezoelectric tube's position. The force is entirely conservative because the average friction of a sinusoidal trace over a period is zero. When the cantilever deflection is increased to 250 nanometers, the friction traces loses its sinusoidal symmetry, but remains conservative. On the downward

[6]For purposes of illustrating physical mechanisms, the lateral frequency of the cantilever was decreased by a factor of 30 for the production of Figure 5-4. All numerical results, however, use the actual cantilever frequency. Appendix E shows and discusses the graphical results for the actual cantilever frequency.

slope, the geometric constraint described by Equation (3.33) forces a rapid decrease in lateral surface force per unit time. Physically, as the sinusoidal potential begins to decrease the surface force, the cantilever and surface spring extension begins to decrease as well. To meet the geometry constraint, the slip distance rapidly increases and thereby further decreasing the surface force. This 'positive' feedback mechanism can also be described energetically. As the slip distance and lateral surface force increase, the surface interaction potential accumulates in the cantilever and contact springs. After the spring reaches its maximum potential, it begins to transfer energy to the surface. This transfer is determined by the surface's potential function and the surface spring's constitutive relation. When the second directional derivative of the potential function is less than the contact stiffness, the tip position remains stable. Mathematically,

$$-\frac{\partial^2 V_{xz}}{\partial x^2} \leq k_s \tag{5.1}$$

Equivalently, Johnson and Woodhouse state that stability is maintained when the nondimensional contact stiffness is greater than 2π.

In Trace 3, the cantilever deflection is 500 nanometers. The nondimensional contact stiffness is 5.5640 and as expected the cantilever tip position is unstable. During the slip process, the surface spring can not keep up with the rapid decrease in the surface potential. As a result, energy is transferred to the cantilever where it is lost in the form of damped oscillation. Energy is also transferred to the surface in the form of phonons. A measure of this type of energy dissipation can be made by comparing the maximum and minimum surface force for each trace. Table 5.2 shows these results. In the first two traces, due

Number	$maxF_x(\mu N)$	$minF_x(\mu N)$	% Loss
1	.37980	-.37980	0.0000e+000
2	1.0051	-1.0050	2.5783e-003
3	2.0187	-2.0179	4.0589e-002
4	3.0074	-2.7777	7.6369e+000
5	3.9785	-2.7160	3.1733e+001

Table 5.2: Maximum and Minimum Forces for Contact Mode Simulations

to the stability condition, the maximum and minimum friction forces are identical within simulation tolerances. In the third trace, the system is just beyond the stability condition

and the magnitude of the minium surface force is a small percentage less than the magnitude of the maximum lateral surface force. A dramatic change occurs for the fourth trace. Almost 8% of the surface force magnitude is lost due to the slip process and almost 32% of the surface force magnitude is lost for the fifth simulation.

Interestingly, the last trace shows a minimum surface force magnitude smaller than the trace just before it. These losses result in an increase in the average friction surface force over a lattice spacing. In other words, for increasing normal force the surface stores an increasing amount of energy.

5.4 Tapping Mode Simulink Model

The tapping mode simulation is similar to the contact mode simulation in that it builds upon El Rifai's tapping mode simulations, but has many implementation features in which the two differ [27]. The main difference is that the lateral dynamics model is coupled to the vertical dynamics model into a single AFM tapping mode Simulink model. Figure 5-5 shows how the block diagram integrates the two models into a single model that finds the values for the lateral surface force. The Piezoelectric Tube-Cantilever Model is identical to the one used in the contact mode model. In addition to its dynamics, the steady state bimorph shaker response is added. Figure 5-6 shows how the results of Equations (2.42), (2.46), (2.48) and (2.49) are superimposed and added to the state space response. The states are used as inputs to the 'computetapping' function which much like 'computecontact' uses the Maugis-Dugdale model to calculate the normal force among other physical quantities[7]. The function also uses a hit crossing block to find when the cantilever velocity is zero. This is used in calculation of the root mean square cantilever amplitude which is then subtracted from the setpoint to create an error signal sent to the controller. The controller takes the same form as the contact mode controller but uses a different value for the PID gain to maintain stability. The 'Computetapping' function also calculates the time in which the cantilever tip has initially 'touched down' to the surface. 'Touched down' is defined as feeling the adhesion and elastic interactions of the surface. Quantitatively, this is defined

[7]The Matlab Code for the function is in Appendix D.3

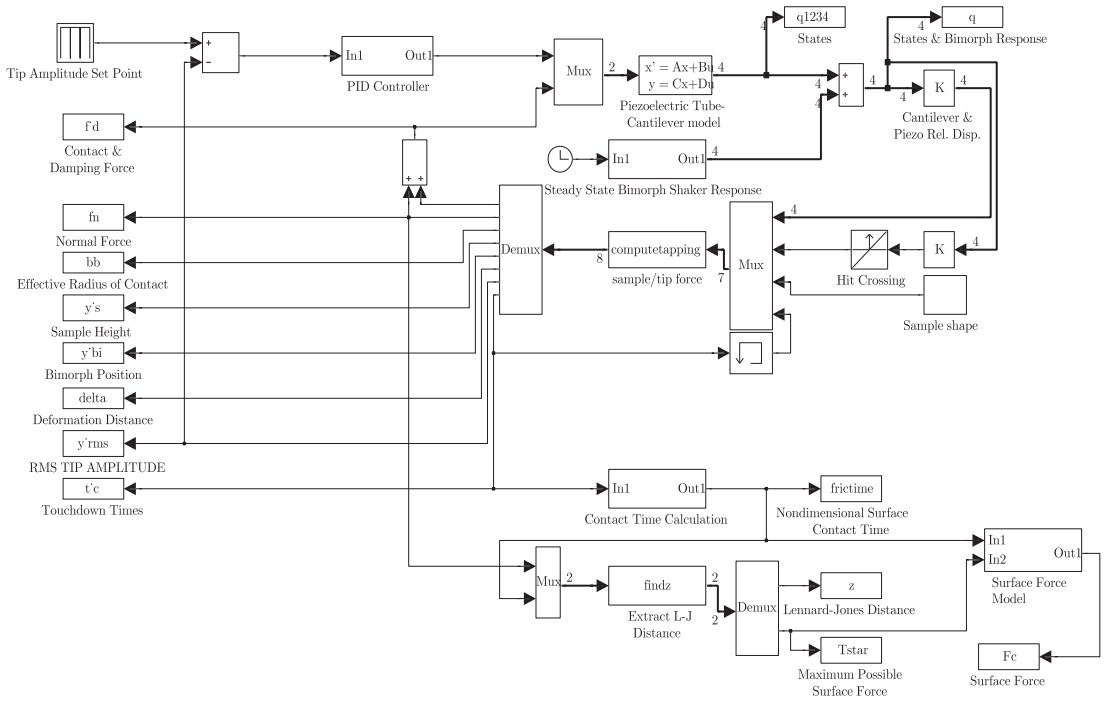

Figure 5-5: A Block Diagram of the Atomic Force Microscope Tapping Mode Model

in the Maugis Dugdale model in terms of the deformation distance δ as:

$$\delta > \delta_o \tag{5.2}$$

δ_o is the deformation distance at the contact area is zero. The touchdown time is used to directly calculate the time in the friction model. Figure 5-7 shows how the calculation is performed in the Contact Time Calculation Block. The time interval in which the cantilever has been in contact is multiplied by a gain that first dimensionalizes the time, and then nondimensionalizes it with respect to the lateral dynamics model. The switch exists such that surface force calculations are only performed when in contact. The output of the block together with the normal force calculation is used as an input to 'findz' function[8]. The function, under the condition of interacting with the surface, first numerically finds the Lennard Jones distance, and then uses it to calculate the amplitude of the lateral surface

[8]The Matlab code for this function is in Appendix D.4.

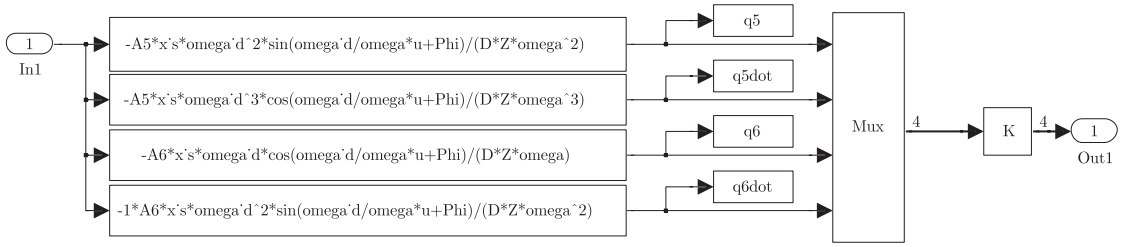

Figure 5-6: A Block Diagram of Steady State Shaker Bimorph Shaker Response

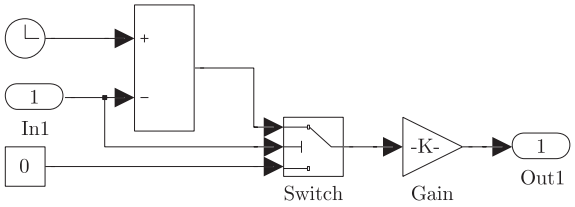

Figure 5-7: A Block Diagram of Lateral Dynamics Model Time Calculation

force function. Both values are sent to the Simulink environment. The maximum surface force together with the lateral dynamics model time are used as inputs to the friction model which is shown in Figure 5-8. A nondimensional constant representing the piezoelectric tube

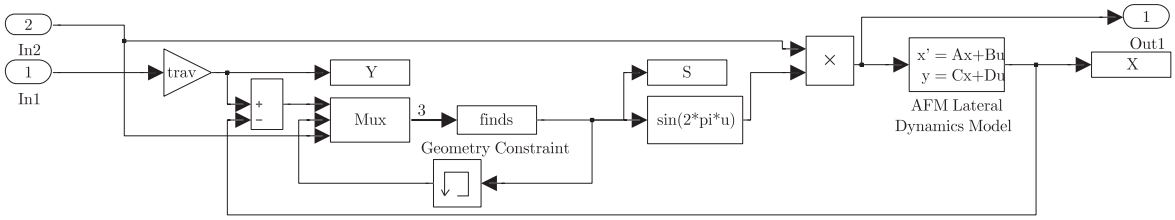

Figure 5-8: A Block Diagram for Tapping Mode Friction Model

velocity is used to calculate the piezoelectric tube postion. It, together, with the cantilever tip position is used as an input to the 'finds' function[9]. The 'finds' function used in tapping

[9]The Matlab code for this function is Appendix D.5.

mode serves the same function as its contact mode counterpart. It, however, must also account for the time varying nature of the surface force amplitude. The function also only operates when the cantilever is interacting with the surface. The slip distance it calculates is then used to calculate the surface force which is used to excite the state space representation of the lateral dynamics of the cantilever.

The tapping mode Simulink model has many of the useful features found in the contact mode Simulink model. Varying samples shapes can be simulated, and transients of the cantilever and piezoelectric tube are captured. It also allows the user to control the root mean square cantilever amplitude set point and the bimorph shaker amplitude. Much like the previous investigation, atomically flat surfaces will be scanned each time. A bimorph shaker amplitude of one nanometer was used in combination with a root mean square cantilever amplitude of 42.426 nanometers.

5.5 Tapping Mode Simulation Procedure

Like the contact mode simulations a fully automated Matlab script was written to initialize and repeatedly run simulations, change simulation parameters, and save pertinent results. First, a parameter file that initialized both vertical and lateral dynamics models was executed. The tapping mode Simulink model was run for 50 nondimensional time units with the lateral dynamics model making calculations for the whole time. This run captures the surface force behavior for approximately the first fifteen taps of the transient response. Relevant data was saved and a second simulation in which scan velocity was varied from five to fifty microns per second was run. The simulation was run for the same length of time, but only data for the first tap was saved. The last simulation captured the lateral surface force behavior of the AFM in its tapping mode steady state. 'ode23s' was chosen as the differential equation solver because it proved to be more robust than 'ode45' in contact mode simulations. A relative and an absolute tolerance of 10^{-4} and 10^{-6} was used respectively.

5.6 Tapping Mode Simulation Results

From the contact mode simulations, it was expected that the tapping mode friction force would depend primarily upon the normal force experienced by the cantilever. The peak normal force was found to vary significantly from tap to tap over the course of the tapping

mode transient. Instead of running many simulations, the data from these taps of varying normal force were used. Figure 5-9 shows a plot of the normal force, Lennard Jones distance, and surface force as a function of time for typical tap. As expected, the plot shows a sharp

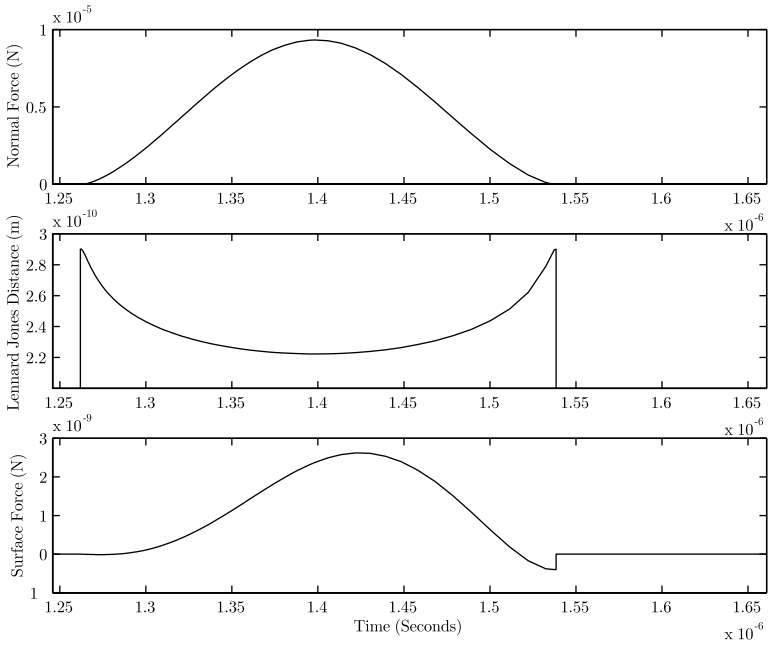

Figure 5-9: Normal Force, Lennard Jones Distance and Friction Force for a Typical Tap

increase and decrease in the normal force as a function of time. It, however, does not show the negative normal force values because they are very small in relation to the maximum normal force values. Numerically, the data shows a minimum normal force value of -22.674 nanoNewtons while the maximum is 8.0878 microNewtons. When the normal force becomes positive, the Lennard Jones is at its equilibrium distance of 2.56Å. Prior to that value, the Lennard Jones distance is greater than that and hence vertically pulls on asperity. After that value, repulsion ensues and the small Lennard Jones distance causes an upward push on the asperity. According to the model, the surface force, like the normal force, is at first negative. The surface force, as expected, then rises sharply with the instantaneously rising normal force. It, however, remains three orders of magnitude smaller than the normal force. The relative magnitudes of the lateral surface force and the normal force in tapping mode can be compared to the contact mode found in the third trace. There, the peak surface force was 2.0187 microNewtons for a similar normal force of 9.9183 microNewtons.

In other words, similar peak normal forces lead to lateral force values that are three orders of magnitude smaller. This result occurs due to the lateral force's sinusoidal dependence on slip distance. In tapping mode, very little slip has occured and so the sine function serves to severely limit the value to which the friction force can rise.

The lateral surface force as a function of piezoelectric tube position while in contact with surface is shown in Figure 5-10. The first fifteen taps of a simulation are shown. Each tap shows a trace of similar shape as in Figure 5-9. At the end of each tap, the piezoelectric tube position returns to zero so that each tap matches the condition of zero lateral force at zero slip distance. As can be seen, the maximum piezoelectric tube displacement is 1.6522 picometers. This is much less than the length of a lattice constant. The increasing surface force effect from the sinusoid is only apparent in the first half of the contact time. In the second half, the cantilever tip is already moving upwards, away from the surface[10].

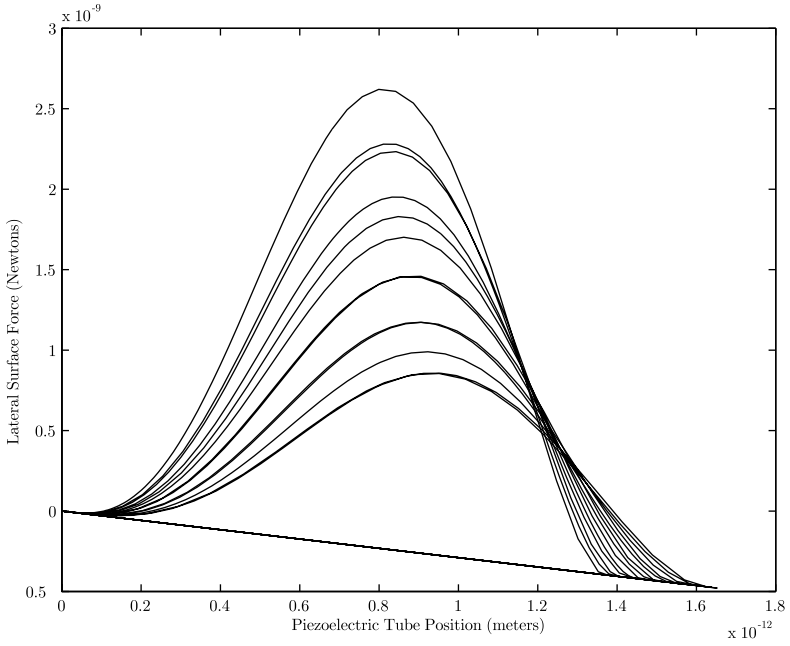

Figure 5-10: Horizontal Surface Force for 15 Taps as a Function of Piezoelectric Tube Displacement

One way to increase the surface interaction is by increasing the contact time during

[10]Because the lateral surface force in simulation is only calculated under the condition $\delta > \delta_o$, the fifteen force traces prematurely stop as opposed to returning back to zero. In other words, if the surface force calculations had been performed for all conditions, the model would show the surface force returning to zero.

tapping. This can be achieved by increasing the velocity of the piezoelectric tube. Figure 5-11 shows five traces for varying scan velocities. The velocity and peak surface interaction force for each trace is summarized in Table 5.3

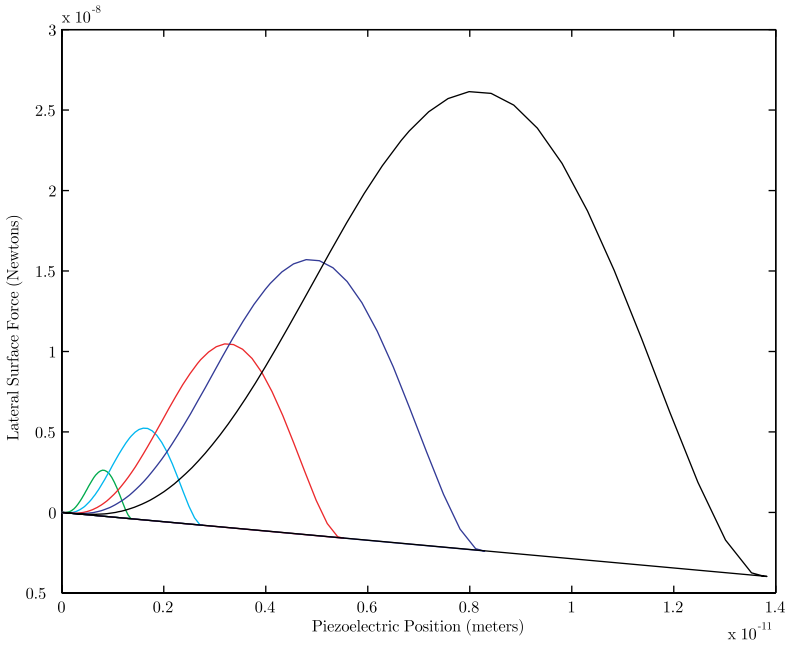

Figure 5-11: Lateral Surface Force as a Function Piezoelectric Tube Displacement for Varying Velocities

Number	Scan Velocity $\mu m/s$	Max $MaxF_xnN$
1	5	2.6201
2	10	5.2367
3	20	10.472
4	30	15.703
5	50	26.147

Table 5.3: Maximum and Minimum Forces for Contact Mode Simulations

The figure shows a direct correlation between scan speed and lateral surface force. Increasing the scan rate gives more time for the lateral dynamics to occur relative to the vertical dynamics. The slip distance then accumulates further causing a larger surface force. If the scan rate were increased beyond 50 microns per second, it is expected that traces similar to those of contact mode would begin to appear.

Thus far, all the tapping mode results have described 'aggressive' taps associated with

transients of the vertical dynamics model. In tapping steady state, each individual tap has less of an impact on the surface than some taps that occur during the transient. Accordingly, peak normal forces are small as well. Figure 5-12 shows a peak normal force of 86.325 nanoNewtons for a typical tap in steady state tapping mode operation of the AFM. It is

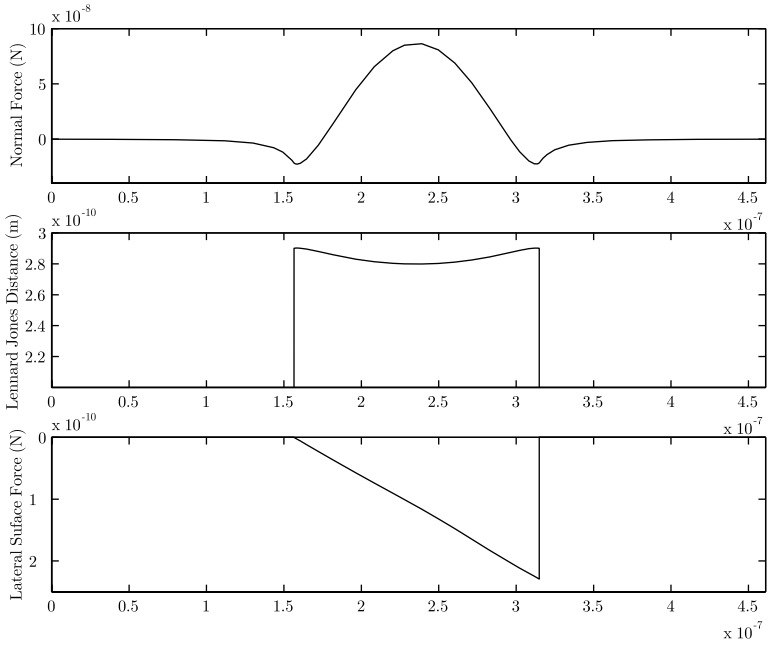

Figure 5-12: Friction Force for 15 Taps as a Function of Piezoelectric Tube Displacement

two orders of magnitude less than 'typical' tap in the transient tap shown earlier. The Lennard Jones distance starts at nearly three angstroms and decreases as the normal force increases. It, however, does not reach the equilibrium distance of $z_o = 2.56\mathring{A}$. This appears to cause the seemingly peculiar result of a surface force that is negative over the entire contact time of that tap. The lateral surface force seemingly adds to the cantilever energy with every tap. In addition, the lateral surface force appears to not just be negative, but it is also negative for small positive normal forces as well.

5.7 Discussion

The validity of the model and its simulation results should be ascertained by comparing it to experimental results. In their absence, general comments on the intuitiveness of the model can be made. First, the contact mode simulation results will be discussed. Next,

the tapping mode results are reviewed. Lastly, a mathematical agreement is proposed to explain the presence of intuitive as well as counterintuitive results.

In contact mode, expanding the Johnson-Woodhouse model to have a height dependence led to intuitive simulation results of the lateral surface force. Greater cantilever deflections caused greater normal forces which were in turn reflected in surface forces of greater magnitude. The expansion also did not destroy the sinusoidal trace used to describe the lateral stick slip surface forces often measured in lateral force AFM measurements.

In tapping mode, the results are less clear. Whereas in some instances they appear to give intuitive results, in others they appear to give counter intuitive ones. For example, 'aggressive' taps – ones with a relatively large normal force yielded the intuitive result of a positive surface force. Another intuitive result found for tapping mode was that the magnitude of the surface force increased with velocity. Stated in another way, that due to increased contact time, in limit of increasing scan speed, tapping mode lateral surface force behavior tended towards contact mode lateral surface force behavior. With these intuitive results, the model's simulations seem to predict counterintuitive forces as well. For example, negative normal forces seem to give negative lateral surface forces. The model also appears to predict negative lateral surface interactions for small positive normal forces. The mix of intuitive and counterintuitive results may suggest operating regions in which the model is invalid and conditions in which it is valid.

Because of the mixture of seemingly intuitive and counterintuitive results, it was hypothesized that the Simulink code accurately simulates regions of the model that intrinsically have counterintuitive results. To gain insight into this hypothesis, a mathematical investigation of the normal and lateral surface force functions was performed. As stated previously, the normal force function is derived from the Lennard Jones potential and given by Equation (3.18). The lateral surface force function is given by Equation (4.3). The point of zero lateral surface force by inspection occurs at z_o. The point of zero normal force can be solved algebraically to be $\sqrt[6]{2}$. The source of the counterintuitive results seem to stem from the fact these two numbers are different. Figure 5-13 shows the lateral surface and the normal forces plotted nondimensionally on the same axes. It shows three distance regions in how the functions relate to each other. Over the interval, $(0, z_o)$, the two function are both positive. The corresponds to the intuitive result of a positive lateral force for a positive normal force. Over the interval $[z_o, \sqrt[6]{2})$, the functions are opposite sign with the normal force

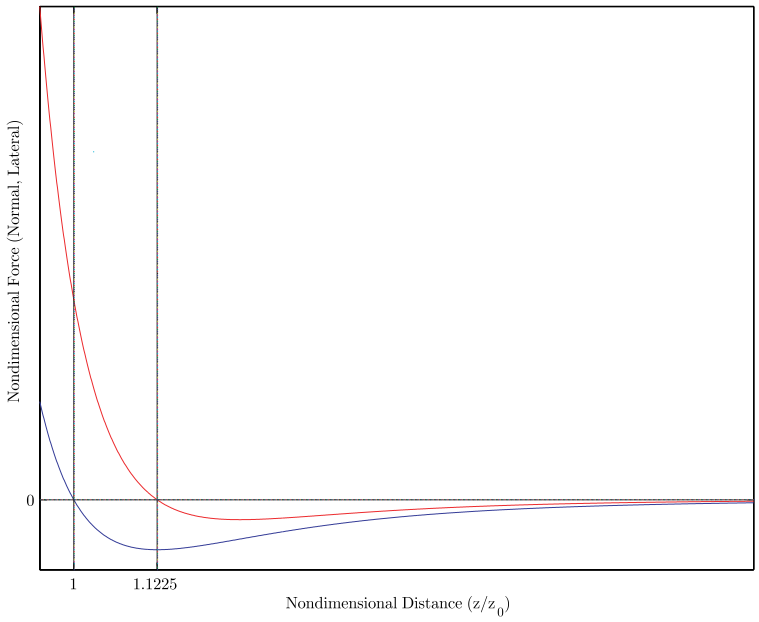

Figure 5-13: Nondimensional Plot of Lateral Surface Force and Normal Force

being greater than zero. Lastly over the interval, $[z_o, \infty]$, the functions are both negative. These two intervals correspond to the counterintuitive results. This mathematical analysis appears to explain the simulation results.

Mathematically, this suggests that the model itself produces some results that are counterintuitive while others that are more intuitive. Physically, this analysis suggests that the model more accurately describes lateral surface forces when elastic contact dominates the normal force. It further suggests that based on intuition the model less accurately predicts lateral surface forces when adhesive contact dominates the normal force.

Chapter 6

Conclusions and Recommendations

6.1 Conclusions

The Johnson-Woodhouse was used to predict the stick-slip lateral surface phenomena measured in AFM force measurments. It was also expanded to predict the dependance of the lateral surface force on the normal force. In this way, the model was developed to apply to both tapping and contact mode. The simulated stick slip behavior described by Johnson and Woodhouse was reproduced for contact mode. The magnitude of the lateral surface force was found to depend on the cantilever deflection/ normal force applied by the surface in contact mode. Similar results were simulated with respect to tapping mode as well. 'Aggressive' taps that had large normal force peaks were found to give positive lateral surface forces. For small positive normal force peaks, as well as for negative normal force peaks, the results appeared to be less intuitive. The model suggests that negative normal forces lead to negative lateral surface forces. It appears to suggest the same for small normal forces as well. Further mathematical analysis of the model showed that the model would predict less intuitive lateral surface force results for atomic distances greater than the equilibrium Lennard Jones distance. The analysis also suggests that the model would predict intuitive results for atomic distances less than the equilibrium Lennard Jones distance or in other words over a regime where elastic contact dominates the normal force. A further tapping mode result was that as the scan velocity increased the lateral surface force increased to resemble contact mode lateral surface forces.

6.2 Recommendations

The most important recommendation is to resolve the counterintuitive results that the model suggests. Literature describes experimental results of lateral surface forces in the regime of primarily elastic contact. Studies involving near contact lateral surface force studies have not been found. Additionally, experimental lateral surface force studies for tapping mode have not been as well. If accurate experimental results can be obtained regarding lateral surface forces in this type of operation of the AFM, it can prove to be very useful in validating the model proposed in this thesis. If such data is not forthcoming, the model must be revised to give more intuitive results. A greater understanding of the surface interactions and their mechanisms will be required.

6.3 Final Thoughts

This thesis uses a model in which many nanoscale surface forces are lumped into a single force which in contact mode experimentally appears to be described by stick slip phenomena. This phenomena, however, is a combination of many different interactions; each having their own physical mechanism. In order to truly gain knowledge of the lateral surface force in the AFM it will eventually become important to understand 1.) the underlying interactions involved and 2.) the mechanisms by which they occur. Such a method might also lead to a greater understanding of the nature of friction which is probably just one of the different interactions that occur between two many atom bodies.

Appendix A

List of Variables

α_n	Simplifying Constant. See Equation (2.20
a	Elastic Contact Area Radius
$a_{1,2,3,4}$	Interaction Potential of Gyalog and Thomas Model Fourier Terms
$\bar{a}$	Nondimensionalized Elastic Contact Area Radius
A	System Dynamics Matrix
$A_{1,2,3,4}$	Nondimensional Cantilever Equation of Motion Forcing Terms Coefficients
A_5	Shaker Acceleration Forcing Term Coefficient
A_6	Shaker Velocity Forcing Term Coefficient
A_c	Cantilever Beam Cross-sectional Area
A_f	Frictional Contact Effective Area
A_p	Piezoelectric Tube Cross-sectional Area
b	Maugis-Dugdale Model Frictional Contact Effective Radius
b_{cx}	Cantilever Beam Damping Coefficient in Lateral Direction
b_{cz}	Cantilever Beam Damping Coefficient in Vertical Direction
b_p	Piezoelectric Damping Coefficient Tuning Constant
b_s	Surface Damping Coefficient
B	System Excitation Matrix
B_n	An Arbitrary Constant
c	Radius of Adhesion Area
$\bar{c}$	Non-dimensionalized Adhesion Area Radius
c_{pn}	nth Mode Piezoelectric Tube Modal Damping Coefficient

C	System Output Matrix
C_p	Piezoelectric Tube Capacitance
δ	Cantilever Tip Deflection Distance
δ_o	Zero Contact Area Cantilever Deflection Distance
d_{31}	Piezoelectric Tube Strain-Voltage Proportionality Constant
D	System Output Excitation Matrix
D_m	Maugis Dugdale Non-Dimensional Displacement
D_r	Electric Displacement-Charge
ϵ	Lennard-Jones Potential Parameter
ϵ_z	Piezoelectric Tube Strain
η	Ratio of Adhesion Contact Radius to Elastic Contact Area
E	Effective Interfacial Youngs Modulus
E_a	Youngs Modulus of Asperity
E_s	Youngs Modulus of Surface
E_c	Youngs Modulus of Cantilever
E_p	Youngs Modulus of Piezoelectric Tube
E_r	Piezoelectric Tube Applied Electric Field
F^*	Maximum Lateral Surface Force
F_f	Tip Sample Friction Force
F_n	Surface to Cantilever Tip Normal Force
$\bar{F}_n$	Non-dimensional Surface to Cantilever Tip Normal Force
F_x	Asperity to Surface Lateral Surface Force
γ	Adhesion Energy Per Unit Area
G	Effective Interfacial Shear Modulus
G_a	Shear Modulus of Asperity
G_s	Shear Modulus of Surface
I	Cantilever Beam Second Moment of Inertia
k_{cx}	Cantilever Stiffnes in Horizontal Direction
k_{czn}	nth Mode Cantilever Tip Modal Stiffness in Vertical Direction
k_{pn}	nth Mode Piezoelectric Tube Modal Stiffness
k_s	Stiffness of Surface in Lateral Direction
k_x	Surface Atoms Relative to Substrate Atoms Stiffness in Lateral Direction

k'_x	Surface Atoms Relative to Each Other Stiffness in Lateral Direction
k_z	Surface Atoms Relative to Substrate Atoms Stiffness in Vertical Direction
K	The Stiffness Matrix of the AFM Cantilever
K_{pv}	Piezoelectric Tube Voltage Proportionality Constant
λ	Nondimensional Maugis Dugdale Parameter
λ_l	Surface Latice Constant
λ_{cn}	Cantilever Beam Wavenumber for nth Mode
l_c	'Dummy' Variable Representing Cantilever Beam Length
l_p	'Dummy' Variable Representing Piezoelectric Tube Length
L	Cantilever Beam Length
L_p	Length of Piezoelectric Tube
μ	Coefficient of Friction
m	Effective Cantilever Mass in the Horizontal Direction
m_{cn}	nth Mode Cantilever Tip Modal Mass in Vertical Direction
m_{pn}	nth Mode Piezoelectric Tube Modal Mass
M_{hold}	Mass of Cantilever and Bimorph Holder
ν_a	Poissons Ratio of Asperity
ν_s	Poissons Ratio of Surface
n	A Simplifying Constant. See Equation (2.5
$)\,\omega_{cxn}$	Cantilever Beam Natural Frequencies in Vertical Direction
ω_{cz}	Cantilever Beam Natural Frequency in Horizontal Direction
ω_d	Driving Frequency of Bimorph Shaker
ω_{pn}	Piezoelectric Tube Natural Frequencies
ϕ	Non-dimensional Parameter Representing Relative Weights of Elasticity & Adhesion
ϕ_s	Phase Angle in Steady State Response Due to Bimorph Shaker
$\psi 1, 2$	The Eigenvalues of the Total System Potential
p	Maugis Dugdale Effective Radius Tuning Parameter
Φ_n	Cantilever Beam Modeshape for nth Mode
Φ_{pn}	Piezoelectric Tube Modeshape for nth Mode
P_a	Force Due to Elastic Contact
P_c	Force Due to Adhesive Contact
q	Non-dimensional modal cantilever tip displacment

$\dot{q}$	Non-dimensional Modal Cantilever Tip Velocity
$\ddot{q}$	Non-dimensional Modal Cantilever Tip Acceleration
q_p	Non-dimensional Modal Piezoelectric Tube Displacment
$\dot{q_p}$	Non-dimensional Modal Piezoelectric Tube Velocity
$\ddot{q_p}$	Non-dimensional Modal Piezoelectric Tube Acceleration
Q_n	nth Mode Cantilever Tip Excitation Term
Q_{pn}	nth Mode Piezoelectric Tube Modal Excitation Term
ρ	Density of Cantilever Beam
ρ_p	Density of Piezoelectric Tube
$\vec{r_c}$	A Coordinate Vector of the Cantilever Tip (Atom)
$\vec{r_i}$	A Coordinate Vector of an Arbitrary Surface Atom
$\vec{r_p}$	A Coordinate Vector of the Piezoelectric Tube
R_a	Asperity Curvature Radius
R_i	Piezoelectric Tube Inner Radius
R_o	Piezoelectric Tube Outer Radius
σ_o	Minimum Lennard Jones Force
σ_z	Piezoelectric Tube Stress in Vertical Direction
s	Horizontal 'Slip' distance
τ	Johnson-Woodhouse Model Nondimensional Time
τ_a	Asperity Shear Strength
τ_e	Effective Interfacial Shear Strength
τ_s	Surface Shear Strength
t	Time
$trav$	Nondimensional Scan Rate, Lateral Velocity
T_n	nth Mode Cantilever Tip Modal Displacement
$\dot{T_n}$	nth Mode Cantilever Tip Modal Velocity
$\ddot{T_n}$	nth Mode Cantilever Tip Modal Acceleration
T_{pn}	nth Mode Piezoelectric Tube Modal Displacement
$\dot{T_{pn}}$	nth Mode Piezoelectric Tube Modal Velocity
$\ddot{T_{pn}}$	nth Mode Piezoelectric Tube Modal Acceleration
V^*	Maximum Interfacial Potential in Lateral Direction
V_T	The Total Potential Between the AFM Cantilever, the Surface

V_x	The Interfacial Surface Potential for a One Dimensional Scan
V_{xy}	The Interfacial Surface Potential for a Two Dimensional Scan
V_z	Interfacial Potential in the Normal Direction
V_{zp}	Piezoelectric Tube Voltage in Vertical Direction
$\bar{V}_{zp}$	Nondimensional Modal Piezoelectric Tube Voltage
$\hat{x}$	Primary Scan Direction Unit Vector
x_c	Cantilever Tip Horizontal Displacement
x_i	Arbitrary Surface Atom Horizontal Displacment
x_p	Piezoelectric Tube Horizontal Displacement
x_s	Surface Stiffness Horizontal Displacement
X	System Dynamics States Vector
$\ddot{X}$	System Dynamics State Derivitives Vector
$\hat{y}$	Secondary Scan Direction Unit Vector
y_c	Cantilever Tip Displacement in the Secondary Scan Direction
z	Vertical Direction Measured from Surface
z_c	Cantilever Tip Relative Displacement
$\dot{z}_c$	Cantilever Tip Velocity
$\ddot{z}_c$	Cantilever Tip Acceleration
z_o	Lennard Jones Potential Critcal Distance
z_p	Piezoelectric Tube Displacement
$\dot{z}_p$	Piezoelectric Tube Velocity
$\ddot{z}_p$	Piezoelectric Tube Acceleration
z_s	Bimorph Shake Relative Displacement
$\dot{z}_s$	Bimorph Shaker Velocity
$\ddot{z}_s$	Bimorph Shaker Acceleration
Z	Simplifying Constant in the Cantilever Steady State Solution (2.44)
$\dot{Z}_s$	Non-dimensional Bimorph Shaker Velocity
$\ddot{Z}_s$	Non-dimensional Bimorph Shaker Acceleration

Appendix B

Parameters for Contact Mode Simulations

A_c	Cantilever Beam Cross-sectional Area	$90pm^2$
b_p	Piezoelectric Damping Coefficient Tuning Constant	35000
b_s	Surface Damping Coefficient	$3 * 10^{-10}$
d_{31}	Piezoelectric Tube Strain-Voltage Proportionality Constant	$-171pm/V$
E_a	Youngs Modulus of Asperity	$169GPa$
E_s	Youngs Modulus of Surface	$59.8GPa$
E_c	Youngs Modulus of Cantilever	$169GPa$
E_p	Youngs Modulus of Piezoelectric Tube	$169GPa$
γ	Adhesion Energy Per Unit Area	$0.1J/m^2$
L	Cantilever Beam Length	$125\mu m$
L_p	Length of Piezoelectric Tube	$25.4mm$
M_{hold}	Mass of Cantilever and Bimorph Holder	$0.5g$
ν_a	Poissons Ratio of Asperity	0.3
ν_s	Poissons Ratio of Surface	0.27
ρ	Density of Cantilever Beam	$2300kg/m^3$
ρ_p	Density of Piezoelectric Tube	$7700kg/m^3$
R_a	Asperity Curvature Radius	$40nm$
R_i	Piezoelectric Tube Inner Radius	$2.675mm$
R_o	Piezoelectric Tube Outer Radius	$3.175mm$

z_o	Lennard Jones Potential Critcal Distance	$2.56\mathring{A}$
z_s	Bimorph Shake Relative Displacement	$1nm$

Appendix C

Contact Mode Matlab Files

C.1 Simulation Automation Script

```
% Authored by Osamah El Rifai
% Revised by  Amro M. Farid
% Program name: simulation
clear all
contactparam
runs=1/D*[1e-6 0.75e-6 0.5e-6 0.25e-6 0.1e-6];
for i=1:5
    height=runs(i)
    sim('contact')
    frictionparam
    sim('friction')
    if i==1
        Ff100=Fc*Tstar;
        y100=Y*lambda_f;
        Fn100=normalforce*pi*w*R;
    end
    if i==2
        Ff75=Fc*Tstar;
        y75=Y*lambda_f;
        Fn75=normalforce*pi*w*R;
```

```
    end
    if i==3
        Ff50=Fc*Tstar;
        y50=Y*lambda_f;
        Fn50=normalforce*pi*w*R;
    end
    if i==4
        Ff25=Fc*Tstar;
        y25=Y*lambda_f;
        Fn25=normalforce*pi*w*R;
    end
    if i==5
        Ff10=Fc*Tstar;
        y10=Y*lambda_f;
        Fn10=normalforce*pi*w*R;
    end
end
i=i+1;
if i==6
    save('contact', ...
        'Ff100', 'Fn100', 'y100', ...
        'Ff75', 'Fn75', 'y75',...
        'Ff50', 'Fn50', 'y50',...
        'Ff25', 'Fn25', 'y25',...
        'Ff10', 'Fn10', 'y10')
    plot(y100,Ff100,'k-')
    hold
    plot(y75,Ff75,'b-')
    plot(y50,Ff50,'r-')
    plot(y25,Ff25,'c-')
    plot(y10,Ff10,'g-')
    hold
```

```
   ylabel('Friction Force (Newtons)')
   xlabel('Piezoelectric Tube Position (Meters)')
end
print -depsc contactresults.eps
```

C.2 Parameter File for AFM Vertical Dynamics Model

```
close all
global nn TT1
nn=0; TT1=0;
%  Authored by Osamah El Rifai
%  Revised by  Amro M. Farid
%  Program name: contactparam
%_____________________________________________________________________
%AFM tapping mode model.  Includes extension of tube and cantilever dynamics.
%_____________________Beam Dimensions and Properties_____________________
L=125e-6;                          %length of beam [m]
roh=2300;                          % density [kg/m^3]
ww=30e-6;                          %width [m]
tt=3e-6;                           %thickness [m]
A=ww*tt;                           %cross-sectional area [m^2]
E=1.69e11;                         %modulus of elasticity [Pa]
I=ww*tt^3/12;                      %moment of inertia [m^4]
nu1=0.3;                           %Poisson ratio
E=E/(1-nu1^2);                     %Corrected Young's Modulus [Pa]
%Converts results from plane stress (thickness<<width to plane strain
%(thickness<< width)
l_t=3e-6;                          %tip length [m]
%____________________Cantilever dynamics_____________________________
gg=[1.875; 4.694; 7.855];          %Guess for characteristic equation
tol=1e-6;                          %tolerance for numerical solution
for hh=1:3
   lambdL(hh)=fzero('cos(x)*cosh(x)+1',gg(hh),1e-6);
   %Characteristic Equation solution.
   %Gives wavenumber for different modes of vibration
end
lambda=lambdL/L;                   %Dimensionless wave number.
```

```
x_t=L;                                  %tip position is at end of cantilever [m]M̂
for i=1:1M̂
   phi(i)=(cos(lambda(i)*x_t)-cosh(lambda(i)*x_t))*(sin(lambda(i)*L)+...M̂
      sinh(lambda(i)*L))+(cos(lambda(i)*L)+cosh(lambda(i)*L))*...M̂
      (sinh(lambda(i)*x_t)-sin(lambda(i)*x_t) );    M̂
   %This is the mode shape equationM̂
   %The following can be verified symbolicly from the extracted mode M̂
   %shape equation above.  M̂
   dphi(i)=lambda(i)*((-sin(lambda(i)*x_t)-sinh(lambda(i)*x_t))*...M̂
      (sin(lambda(i)*L)+sinh(lambda(i)*L))+ (cos(lambda(i)*L)+...M̂
      cosh(lambda(i)*L))*(cosh(lambda(i)*x_t)-cos(lambda(i)*x_t)));M̂
   %dphi(x)/dx.  The derivitive with respect to the length of the cantilever M̂
   %of the mode shape.M̂
   intg_phi(i)=-2*(cos(lambda(i)*L)+cosh(lambda(i)*L))/lambda(i); M̂
   % integeral of phi(x) from 0 to LM̂
   intg_phi2(i)= (sin(lambda(i)*L)+sinh(lambda(i)*L))^2*L; M̂
   % integral of phi(x)^2M̂
   intg_d2ph2(i)= (sin(lambda(i)*L)+sinh(lambda(i)*L))^2*lambda(i)^4*L; M̂
   %integral of (d2phi/dx^2)^2M̂
      % modal parametersM̂
      m(i)=roh*A*intg_phi2(i);          %modal massM̂
      k(i)=E*I*intg_d2ph2(i);           %modal stiffnessM̂
      omega(i)=sqrt(k(i)/m(i));         %modal frequencyM̂
%_____Piezoelongation transfer function dynamics_____M̂
      R_o=0.003175;                     %outer raduis of piezo tube [m]M̂
      R_i=0.002675;                     %inner raduis of piezo tube [m]M̂
      A_p=pi*(R_o^2-R_i^2);             %Cross sectional area of piezetube [m]M̂
      roh_p=7700;                       %density of piezo tube material [kg/m^3]M̂
   sE11=16.4e-12; %piezo mechnical "compliance" at constant electric field [m^2/N)M̂
   d_31=-171e-12;                       %piezo constant [m/V]M̂
      b_p=35000;                        %damping coefficeint [N.s/m^2]M̂
      M_hold=0.5e-3;                    %mass of tip holder [kg]M̂
```

```
    a=sqrt(1/roh_p/sE11);                    %A constant. Simplifies code.M̂
    L_p=25.4e-3;                             %length of piezo tube [m]M̂
w_pn=[1.2388;3.8878]*a/L_p;                  %natural frequencies [rad/s] M̂
%Solve w_pn*L/a*tan(w_pn*L/a)=roh_p*A_p*L_p/M_hold for w_pnM̂
for j=1:1M̂
    m_p(j)=roh_p*A_p*(L_p/2-a/4/w_pn(j)*sin(2*w_pn(j)*L_p/a))+...M̂
    M_hold*(sin(w_pn(j)*L_p/a))^2;    %modal mass of piezo tubeM̂
    k_p(j)=w_pn(j)^2*m_p(j);                 %modal stiffness of piezo tubeM̂
    c_p(j)=b_p*roh_p*A_p*(L_p/2-a/4/w_pn(j)*sin(2*w_pn(j)*L_p/a)); M̂
    %modal damping coefficentM̂
    k_pv(j)=A_p*d_31*sin(w_pn(j)*L_p/a)/sE11/(R_o-R_i); M̂
    %input gain that multiplies the voltage inputM̂
    phi_p(j)=sin(w_pn(j)*L_p/a);             %The Piezo modeshapeM̂
    intg_zphi_p(j)=a^2/w_pn(j).^2/L_p*( sin(w_pn(j)*L_p/a)-...M̂
      w_pn(j)*L_p/a*cos(w_pn(j)*L_p/a)); M̂
    %integral_0 to L_p of z*phi_p(z) dzM̂
    intg_phi_p2(j)=L_p/2-a/4/w_pn(j)*sin(2*w_pn(j)*L_p/a); M̂
    %integral_0 to L_p of (phi_p(z))^2 dzM̂
    endM̂
%_____Damping for Cantilever_____M̂
Q_a=50;M̂
%quality factor of cantilvere in air =1/2/zeta; zeta=damping ratioM̂
b_a=sqrt(k*m)/Q_a/intg_phi2(i); M̂
%air damping coefficient [N.s/m^2], f_a=b_a*dy_total(x,t)/dtM̂
b_cont=3e-10;  M̂
%tip/sample contact damping coefficient [N.s/m], f_c=b_c*dy_total(x_s,t)/dt; M̂
%x_s :location of tip along cantileverM̂
b_s=0;  M̂
%internal damping coefficient [?], proportional to material strain rate, M̂
%f_s=b_s*d^2/dx^2( I* d^3y_relative(x,t)/dx^2dt ); I:cantilever moment of inertiaM̂
intgrl_ph4ph(i)=0; M̂
% integral ( d^4( phi(i) )/dx^4*phi(i) ) from 0 to LM̂
```

```
b(i)=( b_a*intg_phi2(i)  + b_s*I*intgrl_ph4ph(i));M̂
% effective damping coefficient due to all three types of dampingM̂
%_____M̂
%parameters for Maugis contact modelM̂
w=0.2;                          %surface energy [J/m^2]M̂
R1= 40e-9;                      %cantilever probe raduis of curveture [m]M̂
R2=40e-9;                       %sample raduis of curveture [m]M̂
R=(1/R1+1/R2)^(-1);             %REDUCED RADUISM̂
E1=1.69e11;                     %tip Young modulus of elasticityM̂
E2=5.98e10;                     %sample modulus of elasticityM̂
nu2=0.27;                       %Poisson's ratio of sampleM̂
E_str=( (1-nu1^2)/E1+(1-nu2^2)/E2)^(-1);%REDUCED MODULUS OF ELASTTICITYM̂
H=1e-19;                        %Hackermen constant [J]M̂
z_o=2.56e-10;                   %equilibruim separation in Lennard-Jones potential [m]M̂
tau=1;                          %Effective shear strength of materialM̂
mu=(R*w^2/E_str^2/z_o^3)^(1/3);M̂
lambd=1.16*mu;                  %nondimensional parameterM̂
P_o=-2+8*lambd*(pi-2)/9/pi*( sqrt(4*lambd^4*(pi-2)^2+9*pi*lambd)-2*lambd^2*(pi-2));M̂
delta_o=-8/9/pi*(sqrt(4*lambd^4*(pi-2)^2+9*pi*lambd)-2*lambd^2*(pi-2));M̂
zeta_o=delta_o - sqrt(-H*R/6/(P_o*pi*w*R))/(9*pi^2*w^2*R/16/E_str^2)^(1/3);M̂
D=(9*pi^2*w^2*R/16/E_str^2)^(1/3); %nondimensional displacement from Maugis contact modelM
n=.4;                           %Effective area weighting factorM̂
%_____Scan Parameters_____M̂
% bimorph parameters x_s(t)= x_s cos(omega_d*t)M̂
x_s=0;                          M̂
omega_d=0.993*sqrt(k/m);        %driving frequency [rad/s]M̂
ypo=.1*l_t/D;                   %initial position of piezo tube free end [m]M̂
v=5e-6;                         %scan rate [m/s]M̂
V=v/D/omega;                    %non-dimensional scan rateM̂
%%averaging period for RMS value of measured catilever amplitude relative to its baseM̂
T=40/omega_d*omega;M̂
pi_zero=-0.3;                   %PI controller zeroM̂
```

```
pi_gain=.5e-6;                    %PI controller gain in tapping mode
M
%_____Non-dimensional State Space Representation_____M
% state space model, states are q, dq/dt, qp, qp/dt   M
% where modal  solution cantilever deflection=Sum {phi_i(x)*q(t)}  M
% and for cantilever  deflection = ypM
i=1;                              %first mode of cantilever and piezo onlyM
%For clairification   Piezo has m_p, c_p, k_p.  Cantilever has m(i), k(i), beff(i)M
A_ol=[[0 1 0 0]; M
   [-k(i)/m(i)/omega^2,  -b(i)/m(i)/omega,...M
        roh*A/m(i)*intg_phi(i)*k_p/m_p/omega^2,...M
        (roh*A/m(i)*intg_phi(i)*c_p/m_p-b_a/m(i)*intg_phi(i))/omega];M
   0 0 0 1; M
   [0 0 -k_p/m_p/omega^2, -c_p/m_p/omega]]; %substituted yp dynamics inM
B_ol=[[0 0];M
   [-roh*A/m(i)*intg_phi(i)*k_pv/m_p/omega^2/D  phi(i)/m(i)*pi*w*R/omega^2/D];M
   [0 0];M
   [k_pv/(m_p*omega^2*D) 0]];M
C_q=[1 0 0 0];                    %q(t) as outputM
C_x=[phi(i) 0 0 0];               %x(t) as output: yj(t) as output: rel.  M
                                  %def. at tip w.r.t. piezoM
C_xa=[phi(i) 0 1 0];              %xa(t) absolute defelection at tip M
C_dq=dphi(i)*C_q;                 %dq(t)/dx as output: slope at tipM
D_ol=0;M
endM
%_____Sample surface_____M
xo=0/D;                           %[m]M
x1=35e-9/D;                       %[m]M
yo=0/D;                           %[m]M
y1=50.e-9/D;                      %[m]
```

C.3 Computecontact Function

```
function [sys,x0,str,ts]=computecontact(t,x,u,flag,L,T,phi,...
    H,E_str,z_o,mu,lambd,P_o,delta_o,zeta_o,w,R,b_cont,D,xo,...
    x1,yo,y1,v,x_s, omega,omega_d,n,l_t)
global nn TT1
%
% % Written by: Osamah El Rifai
% % Revised by: Amro M. Farid
% Program name: computecontact
% 
%
switch flag % return structure and initial conditions
    sizes=simsizes;
    sizes.NumContStates=1;
    sizes.NumDiscStates=1;
    sizes.NumOutputs=6;
    sizes.NumInputs=5;
    sizes.DirFeedthrough=1;
    sizes.NumSampleTimes=2;
    
    sys=simsizes(sizes);
    
x0=[0;0]; %initial conditions
str=[]; % string
ts=[0 0;T 0]; % smapling (time,offset) pair for continuous and discrete states
set_param(gcb,'UserData',x0(1)); % initialize to store state no. 1 in UserData
case abs(flag)==1 % return derivatives of states
        
    dx(1,1)=u(1)^2; % integral of relative delection of cantilever wrt piezo to
```

```
                %be used in computing rms oscillation amplitude
  sys=dx;
  
**elseif flag** == 2 % update discrete state
 
**elseif flag** == 3 % returns system states as outputs in vector sys
delta=u(5)−u(2)−u(1);%l_t/D+
**if** delta>0.995∗delta_o,
  % Initial guess
    m=25;                                                              40
    aa=25;
    %initialize
    i=1;
    f(i)=1; g(i)=1; dm(i)=1; da(i)=1;

    while abs(f(i))>=1e−8 & abs(g(i))>= 1e−8 & abs(dm(i))>=1e−8 & abs(da(i))>=1e−8
    i=i+1;
  f(i)=lambd∗aa^2/2∗( sqrt(m^2−1)+(m^2−2)∗asec(m)) + ...
    4∗lambd^2∗aa/3∗(1−m+sqrt(m^2−1)∗asec(m))−1;
  dfda=lambd∗aa∗( sqrt(m^2−1)+(m^2−2)∗asec(m) )+ ...                   50
    4/3∗lambd^2∗( 1−m+sqrt(m^2−1)∗asec(m) );
  dfdm=lambd∗aa^2/2∗( m/sqrt(m^2−1) + 2∗m∗asec(m)+...
    (m^2−2)/m/sqrt(m^2−1))+...
    4/3∗lambd^2∗aa∗(−1+m∗asec(m)/sqrt(m^2−1)+1/m);
        % imposing delta as the known variable
        g(i)=aa^2−4∗lambd∗aa/3∗sqrt(m^2−1)−delta;
        dgda=2∗aa − 4/3∗lambd∗sqrt(m^2−1);
        dgdm=−4/3∗lambd∗aa∗m/sqrt(m^2−1);
        %solving system of linear algebraic equations 
        DFG=[dfda dfdm;dgda dgdm];                                      60
        B=[−f(i);−g(i)];
        dadm=DFG\B;
```

```
                da(i)=dadm(1);M̂
                dm(i)=dadm(2);M̂
                aa=aa+da(i);M̂
        m=m+dm(i);M̂
        cc=m*aa;M̂
        bb=aa+n*(cc-aa);M̂
          endM̂
          P=aa^3-lambd*aa^2*( sqrt(m^2-1) +m^2*asec(m));M̂                    70
          P_damp= -(b_cont*(u(3)+u(4)))/pi/R/w;M̂
M̂
elseif delta <=0.995*delta_o, M̂
   P=P_o*(delta_o+zeta_o)^2/(delta+zeta_o)^2;M̂
   P_damp=0;M̂
   m=0;M̂
   bb=0;M̂
endM̂
          M̂
          y_s=u(5);M̂                                                        80
          sys=[P_damp;M̂
          P;M̂
          bb;M̂
          y_s;M̂
          delta;M̂
        u(1)];M̂
elseM̂
        sys=[ ];M̂
end
```

C.4 Parameter File for Friction Model

```
% Authored by: Amro M. Farid
% Program name: frictionparam
%____________________Johnson Friction Parameters____________________________
e=12;                          %Lennard Jones Energy Parameter [eV]
eV_J=1.60217733e-19;           %Conversion Factor eV->J
lambda_f=1.75*z_o;             %Lattice Constant [m]
zeta_f=.1;                     %Damping Ratio
kl=E*A/(4*L);                  %Cantilever Stiffness
ml=roh*A*L/3;                  %Effective Cantilever Mass
omega_x=sqrt(kl/ml);           %Lateral Cantilever Natural Frequency
stifrat=3/4;                   %Ratio of Stiffnesses
kc=stifrat*kl;                 %Contact Stiffness
M
sfn=size(fn);                  %Size of Normal Force Vector from Previous Simulation
sfn=sfn(1);                    %Size of Normal Force Vector
normalforce=fn(sfn);                        %Normal Force
fns=num2str(fn(sfn)*pi*w*R);   %A String of the Dimensional Force Quantity
es=num2str(e*eV_J);            %A String for Lennard Jones Parameter
zos=num2str(z_o);              %A String for Lennard Jones Equilibrium Distance
func=['24*' es '*(2*(x.^13)-(x.^7))-' fns '*' zos];M
a=fzero(func,1,1e-6)M
z=z_o/a;M
Tstar=4*e*(a^12-a^6)*eV_J*2*pi/lambda_fM
%Maximum Friction Force
Kc=kc*lambda_f/Tstar           %Nondimensional Contact Stiffness
Kl=kl*lambda_f/Tstar           %Nondimensional Cantilever Stiffness
trav=v/(lambda_f*omega_x);     %Nondimesional piezo velocity
```

C.5 Finds Function

```
function [sys,x0,str,ts]=finds(t,x,u,flag,Kc)M̂
global nn TT1M̂
%M̂
% %  Written by: Amro M. Farid M̂
%  Program name: finds                                    M̂
% M̂
%M̂
M̂
if flag==0                    % return structure and initial conditionsM̂
   sizes=simsizes;M̂                                                    10
   sizes.NumContStates=0;M̂
   sizes.NumDiscStates=0;M̂
   sizes.NumOutputs=1;M̂
   sizes.NumInputs=2;M̂
   sizes.DirFeedthrough=1;M̂
   sizes.NumSampleTimes=1;M̂
   M̂
   sys=simsizes(sizes);M̂
M̂
      %x0=[0 0];              %initial conditionsM̂                      20
      str=[];                 % stringM̂
   ts=[0 0];                % smapling (time,offset) pair for M̂
                            % continuous and discrete statesM̂
elseif flag ==1M̂
   sys=0;M̂
elseif flag == 3              % returns system states as outputs in vector sysM̂
   kcstring=num2str(Kc);M̂
   YminusX=num2str(u(1));M̂
   func=[YminusX '-x-sin(2*pi*x)/' kcstring];M̂
   s=fzero(func,u(2),1e-6);M̂                                           30
```

sys=s; M̂

elseM̂

sys=[ ];M̂

end M̂

Appendix D

Contact Mode Matlab Files

D.1 Simulation Automation Script

```
% Authored by Amro M. Farid
% Program name: simulation
clear all
tappingparam
endtime=50;
sim('tapping')
sfc=size(Fc);
for i=1:sfc
   if Fc(i)~=0
      pos1=i;
      break
   end
end
for i=i:sfc
   if Fc(i)==0
      pos2=i;
      break
   end
end
Time=t/omega;
```

```
subplot(3,1,1);M̂
plot(Time(pos1−30:pos2+10),fn(pos1−30:pos2+10)∗pi∗w∗R);M̂
axis([Time(pos1−30) Time(pos2+10) 0 1e−5]);M̂
ylabel('Normal Force (N)');M̂
subplot(3,1,2);M̂
plot(Time(pos1−30:pos2+10),z(pos1−30:pos2+10))M̂
axis([Time(pos1−30) Time(pos2+10) 2e−10 3e−10]);M̂
ylabel('Lennard Jones Distance (m)');M̂
subplot(3,1,3);M̂
plot(Time(pos1−30:pos2+10),Fc(pos1−30:pos2+10));M̂
axis([Time(pos1−30) Time(pos2+10) −1e−9 3e−9]);M̂
ylabel('Friction Force (N)');M̂
xlabel('Time (Seconds)');M̂
print tapresults1.epsM̂
figureM̂
plot(Y∗lambda_f,Fc)M̂
xlabel('Piezoelectric Tube Position (meters)')M̂
ylabel('Friction Force (Newtons)')M̂
print tapresults2.epsM̂
save halfrunM̂
M̂
clear allM̂
tappingparamM̂
runs=[5e−6 1e−5 2e−5 3e−5 5e−5];M̂
for i=1:5M̂
    v=runs(i);M̂
    V=v/D/omega;M̂
    trav=v/(lambda_f∗omega_x);M̂
    sim('tapping')M̂
    if i==1M̂
        Ff1=Fc;M̂
        Y1=Y∗lambda_f;M̂
```

```
    Fn1=fn*pi*w*R;M̂
    Z1=z;M̂
    Time1=t/omega;M̂
end M̂
if i==2M̂
    Ff2=Fc;M̂
    Y2=Y*lambda_f;M̂
    Fn2=fn*pi*w*R;M̂
    Z2=z;M̂
    Time2=t/omega;M̂
end M̂
if i==3M̂
    Ff3=Fc;M̂
    Y3=Y*lambda_f;M̂
    Fn3=fn*pi*w*R;M̂
    Z3=z;M̂
    Time3=t/omega;M̂
end M̂
if i==4M̂
    Ff4=Fc;M̂
    Y4=Y*lambda_f;M̂
    Fn4=fn*pi*w*R;M̂
    Z4=z;M̂
    Time4=t/omega;M̂
end M̂
if i==5M̂
    Ff5=Fc;M̂
    Y5=Y*lambda_f;M̂
    Fn5=fn*pi*w*R;M̂
    Z5=z;M̂
    Time5=t/omega;M̂
end   M̂
```

```
    sfc=size(Fc);
    for j=1:sfc
        if Fc(j)~=0
            pos1(i)=j;
            break
        end
    end
    for j=j:sfc
        if Fc(j)==0
            pos2(i)=j;
            break
        end
    end
end
figure
save tapping
plot(Y1((pos1(1)-30):pos2(1)+10),Ff1((pos1(1)-30):pos2(1)+10),'g-')
hold
plot(Y2((pos1(2)-30):pos2(2)+10),Ff2((pos1(2)-30):pos2(2)+10),'c-')
plot(Y3((pos1(3)-30):pos2(3)+10),Ff3((pos1(3)-30):pos2(3)+10),'r-')
plot(Y4((pos1(4)-30):pos2(4)+10),Ff4((pos1(4)-30):pos2(4)+10),'b-')
plot(Y5((pos1(5)-30):pos2(5)+10),Ff5((pos1(5)-30):pos2(5)+10),'k-')
hold
xlabel('Piezoelectric Position (meters)')
ylabel('Friction Force (Newtons)')
print -depsc tapresults3.eps
clear all
tappingparam
settle=3000;
endtime=50+settle;
sim('tapping')
```

```
sfc=size(Fc);
for i=1:sfc
    if Fc(i)~=0
        pos1=i;
        break
    end
end
for i=i:sfc
    if Fc(i)==0
        pos2=i;
        break
    end
end
Time=t/omega;
Time=Time-Time(pos1-10);
subplot(3,1,1);
plot(Time(pos1-10:pos2+10),fn(pos1-10:pos2+10)*pi*w*R);
axis([Time(pos1-10) Time(pos2+10) -0.4e-7 1e-7]);
ylabel('Normal Force (N)');
subplot(3,1,2);
plot(Time(pos1-10:pos2+10),z(pos1-10:pos2+10))
axis([Time(pos1-10) Time(pos2+10) 2e-10 3e-10]);
ylabel('Lennard Jones Distance (m)');
subplot(3,1,3);
plot(Time(pos1-10:pos2+10),Fc(pos1-10:pos2+10));
axis([Time(pos1-10) Time(pos2+10) -2.5e-10 0]);
ylabel('Friction Force (N)');
save a10set60s3000
print tapresults4.eps
```

D.2 Parameter File for AFM Tapping Mode Model

```
% Authored by Osamah El Rifai
% Revised by  Amro M. Farid
% Program name: tappingparam
close all
global nn TT1
nn=0; TT1=0;
%_____________________________________________________________________
%AFM tapping mode model. Includes extension of tube and cantilever dynamics.
%_____________________Beam Dimensions and Properties_____________________
L=125e-6;                   %length of beam [m]
roh=2300;                   %density [kg/m^3]
ww=30e-6;                   %width [m]
tt=3e-6;                    %thickness [m]
A=ww*tt;                    %cross-sectional area [m^2]
E=1.69e11;                  %modulus of elasticity [Pa]
I=ww*tt^3/12;               %moment of inertia [m^4]
nu1=0.3;                    %Poisson ratio
E=E/(1-nu1^2);              %Corrected Young's Modulus [Pa]
%Converts results from plane stress (thickness<<width to plane strain (thickness<< width)
l_t=3e-6;                   %tip length [m]
%_____________________Cantilever dynamics_____________________
gg=[1.875; 4.694; 7.855];   %Guess for characteristic equation
tol=1e-6;                   %tolerance for numerical solution
for hh=1:3
   lambdL(hh)=fzero('cos(x)*cosh(x)+1',gg(hh),1e-6);%Characteristic solution.
   %Gives wavenumber for different modes of vibration
```

```
end
M
lambda=lambdL/L;                    %Dimensionless wave number.M
x_t=L;                              %tip position is at end of cantilever [m]M
M
for i=1:1M
   phi(i)=(cos(lambda(i)*x_t)-cosh(lambda(i)*x_t))*(sin(lambda(i)*L)+...M
      sinh(lambda(i)*L))+(cos(lambda(i)*L)+cosh(lambda(i)*L))*(sinh(lambda(i)*x_t)-...M
      sin(lambda(i)*x_t) ) ;  %This is the mode shape equationM
   M                                                                    40
      %The following can be verified symbolicly from the extracted mode shape equation above.  M
   M
   dphi(i)=lambda(i)*((-sin(lambda(i)*x_t)-sinh(lambda(i)*x_t))*(sin(lambda(i)*L)+...M
      sinh(lambda(i)*L))+ (cos(lambda(i)*L)+cosh(lambda(i)*L))*(cosh(lambda(i)*x_t)-...M
      cos(lambda(i)*x_t)));M
   %dphi(x)/dx.  The derivitive with respect to the length of the cantilever M
   %of the mode shape.M
   M
   intg_phi(i)=-2*(cos(lambda(i)*L)+cosh(lambda(i)*L))/lambda(i); M
   % integeral of phi(x) from 0 to LM                                   50
   M
   intg_phi2(i)= (sin(lambda(i)*L)+sinh(lambda(i)*L))^2*L; % integral of phi(x)^2M
   M
   intg_d2ph2(i)= (sin(lambda(i)*L)+sinh(lambda(i)*L))^2*lambda(i)^4*L; M
   %integral of (d2phi/dx^2)^2M

      % modal parametersM
      m(i)=roh*A*intg_phi2(i);      %modal massM
      k(i)=E*I*intg_d2ph2(i);       %modal stiffnessM
      omega(i)=sqrt(k(i)/m(i));     %modal frequencyM                  60
M
%_____Piezoelongation transfer function dynamics_____M
```

```
R_o=0.003175;                          %outer raduis of piezo tube [m]M̂
R_i=0.002675;                          %inner raduis of piezo tube [m]M̂
A_p=pi*(R_o^2-R_i^2);      %Cross sectional area of piezetube [m]M̂
roh_p=7700;                            %density of piezo tube material [kg/m^3]M̂
sE11=16.4e-12;          %piezo mechnical "compliance" at constant electric field [m^2/N)M̂
d_31=-171e-12;                  %piezo constant [m/V]M̂
b_p=35000;                                  %damping coefficeint [N.s/m^2]M̂
M_hold=0.5e-3;                         %mass of tip holder [kg]M̂
a=sqrt(1/roh_p/sE11);      %A constant. Simplifies code.M̂
L_p=25.4e-3;                           %length of piezo tube [m]M̂
w_pn=[1.2388;3.8878]*a/L_p;%natural frequencies [rad/s] M̂
%Solve w_pn*L/a*tan(w_pn*L/a)=roh_p*A_p*L_p/M_hold for w_pnM̂
for j=1:1M̂
  m_p(j)=roh_p*A_p*(L_p/2-a/4/w_pn(j)*sin(2*w_pn(j)*L_p/a))+...M̂
    M_hold*(sin(w_pn(j)*L_p/a))^2; %modal mass of piezo tubeM̂
  M̂
  k_p(j)=w_pn(j)^2*m_p(j);                %modal stiffness of piezo tubeM̂
  M̂
  c_p(j)=b_p*roh_p*A_p*(L_p/2-a/4/w_pn(j)*sin(2*w_pn(j)*L_p/a)); M̂
  %modal damping coefficentM̂
  M̂
  k_pv(j)=A_p*d_31*sin(w_pn(j)*L_p/a)/sE11/(R_o-R_i); M̂
  %input gain that multiplies the voltage inputM̂
  M̂
  phi_p(j)=sin(w_pn(j)*L_p/a);   %The Piezo modeshapeM̂
  M̂
  intg_zphi_p(j)=a^2/w_pn(j).^2/L_p*( sin(w_pn(j)*L_p/a)-...M̂
    w_pn(j)*L_p/a*cos(w_pn(j)*L_p/a)); M̂
  %integral_0 to L_p of z*phi_p(z) dzM̂
  M̂
  intg_phi_p2(j)=L_p/2-a/4/w_pn(j)*sin(2*w_pn(j)*L_p/a); M̂
  %integral_0 to L_p of (phi_p(z))^2 dzM̂
```

endM̂

M̂

%_____Damping for Cantilever_____M̂

Q_a=50;M̂

%quality factor of cantilvere in air =1/2/zeta; zeta=damping ratioM̂

M̂

b_a=**sqrt**(k∗m)/Q_a/intg_phi2(**i**); M̂

%air damping coefficient [N.s/m^2], f_a=b_a∗dy_total(x,t)/dtM̂

M̂

b_cont=3e−10; M̂

%tip/sample contact damping coefficient [N.s/m], f_c=b_c∗dy_total(x_s,t)/dt; M̂

%x_s :location of tip along cantileverM̂

M̂

b_s=0; M̂

%internal damping coefficient [?], proportional to material strain rate, M̂

%f_s=b_s∗d^2/dx^2(I∗ d^3y_relative(x,t)/dx^2dt); I:cantilever moment of inertiaM̂

M̂

intgrl_ph4ph(**i**)=0; M̂

% integral (d^4(phi(i))/dx^4∗phi(i)) from 0 to LM̂

M̂

b(**i**)=(b_a∗intg_phi2(**i**) + b_s∗I∗intgrl_ph4ph(**i**));M̂

% effective damping coefficient due to all three types of dampingM̂

M̂

%_____M̂

M̂

%parameters for Maugis contact modelM̂

w=0.2; *%surface energy [J/m^2]M̂*

R1= 40e−9; *%cantilever probe raduis of curveture [m]M̂*

R2=40e−9; *%sample raduis of curveture [m]M̂*

R=(1/R1+1/R2)^(−1); *%REDUCED RADUISM̂*

E1=1.69e11; *%tip Young modulus of elasticityM̂*

E2=5.98e10; *%sample modulus of elasticityM̂*

```
nu2=0.27;                                   %Poisson's ratio of sampleM̂
E_str=( (1−nu1^2)/E1+(1−nu2^2)/E2)^(−1);  M̂
%REDUCED MODULUS OF ELASTTICITYM̂
H=1e−19;                                    %Hackermen constant [J]M̂
z_o=2.56e−10;                               %equilibruim separation in M̂
                                            %Lennard-Jones potential [m]M̂
tau=1;                                      %Effective shear strength of materialM̂
M̂
mu=(R∗w^2/E_str^2/z_o^3)^(1/3);M̂
lambd=1.16∗mu;                              %nondimensional parameterM̂
M̂
P_o=−2+8∗lambd∗(pi−2)/9/pi∗( sqrt(4∗lambd^4∗(pi−2)^2+9∗pi∗lambd)−2∗lambd^2∗(pi−2));M̂
delta_o=−8/9/pi∗(sqrt(4∗lambd^4∗(pi−2)^2+9∗pi∗lambd)−2∗lambd^2∗(pi−2));M̂
zeta_o=delta_o − sqrt(−H∗R/6/(P_o∗pi∗w∗R))/(9∗pi^2∗w^2∗R/16/E_str^2)^(1/3);M̂
M̂
D=(9∗pi^2∗w^2∗R/16/E_str^2)^(1/3); % nondimensional displacement from Maugis contact model
M̂
n=.4;                                       %Effective area weighting factorM̂
%_____Scan Parameters_____M̂
% bimorph parameters x_s(t)= x_s cos(omega_d∗t)M̂
x_s=10e−10;                                 M̂
omega_d=0.993∗sqrt(k/m);    %driving frequency [rad/s]M̂
ypo=l_t/D;                                  %initial position of piezo tube free end [m]M̂
v=5e−6;                                     %scan rate [m/s]M̂
V=v/D/omega;                                %non-dimensional scan rateM̂
%%averaging period for RMS value of measured catilever amplitude relative to its baseM̂
M̂
T=40/omega_d∗omega;M̂
pi_zero=−0.3;                               %PI controller zeroM̂
pi_gain=1e−4;                               %PI controller gain in tapping modeM̂
M̂
M̂
```

```
%_____Simplification of Terms _____M̂
A1=roh*A*intg_phi*phi*k_p/(m*m_p);          %Solution CoefficientM̂
A5=-1*roh*A*omega^2*intg_phi;                %Solution CoefficientM̂
A6=-1*b*omega*intg_phi;                      %Solution CoefficientM̂
Z=((k-m*omega_d^2)^2+(b*omega_d)^2)^.5; %Cantilever ImpedanceM̂
Phi=atan2(b*omega_d,k-m*omega_d^2);          %Phase AngleM̂
M̂
%_____Non-dimensional State Space Representation_____M̂
% state space model, states are q, dq/dt, qp, qp/dt  M̂
% where modal  solution cantilever deflection=Sum {phi_i(x)*q(t)} M̂
% and for cantilever  deflection = ypM̂
M̂
i=1;                                         %first mode of cantilever and piezo onlyM̂
M̂
%For clairification   Piezo has m_p, c_p, k_p.  Cantilever has m(i), k(i), beff(i)M̂
A_ol=[[0 1 0 0]; M̂
   [-k(i)/m(i)/omega^2,  -b(i)/m(i)/omega,...M̂
        roh*A/m(i)*intg_phi(i)*k_p/m_p/omega^2,...M̂
        (roh*A/m(i)*intg_phi(i)*c_p/m_p-b_a/m(i)*intg_phi(i))/omega];M̂
   0 0 0 1; M̂
   [0 0 -k_p/m_p/omega^2, -c_p/m_p/omega]];     %substituted yp dynamics inM̂
M̂
B_ol=[[0 0];M̂
   [-roh*A/m(i)*intg_phi(i)*k_pv/m_p/omega^2/D  phi(i)/m(i)*pi*w*R/omega^2/D];M̂
   [0 0];M̂
   [k_pv/(m_p*omega^2*D) 0]];M̂
M̂
C_q=[1 0 0 0];                          %q(t) as outputM̂
C_x=[phi(i) 0 0 0]; %x(t) as output: yj(t) as output: rel. def. at tip w.r.t. piezoM̂
C_xa=[phi(i) 0 1 0];            %xa(t) absolute defelection at tip M̂
C_dq=dphi(i)*C_q;                       %dq(t)/dx as output: slope at tipM̂
D_ol=0;M̂
```

endM̂

M̂

%_____Sample surface_____M̂

xo=20e−9/D; *%[m]M̂*

x1=35e−9/D; *%[m]M̂*

yo=0/D;M̂

y1=50.e−9/D; *%[m]M̂*

lambda_f=2∗z_o; *%Lattice Constant [m]M̂*

M̂

%_____Johnson Friction Parameters_____M̂

t_c=0;M̂

contact=0;M̂

settle=0.5;M̂

endtime=10;M̂

z=.52∗z_o;M̂

zeta_f=.1;M̂

kl=E∗A/L;M̂

ml=roh∗A∗L/3;M̂

omega_x=**sqrt**(kl/ml);M̂

e=12;M̂

eV_J=1.60217733e−19;M̂

stifrat=3/4;M̂

kc=stifrat∗klM̂

trav=v/(lambda_f∗omega_x);

D.3 Computetapping Function

```
function [sys,x0,str,ts]=computetapping(t,x,u,flag,L,T,phi,H,E_str,z_o,mu,lambd,P_o,...M̂
    delta_o,zeta_o,w,R,b_cont,D,xo,x1,yo,y1,v,x_s, omega,omega_d,n,l_t)M̂
global nn TT1M̂
%M̂
%  Authored by Osamah El RifaiM̂
%  Revised by  Amro M. FaridM̂
%  Program name: computetappingM̂
M̂
if flag==0    % return structure and initial conditionsM̂
    sizes=simsizes;M̂                                                    10
    sizes.NumContStates=1;M̂
    sizes.NumDiscStates=1;M̂
    sizes.NumOutputs=8;M̂
    sizes.NumInputs=7;M̂
    sizes.DirFeedthrough=1;M̂
    sizes.NumSampleTimes=2;M̂
    M̂
    sys=simsizes(sizes);M̂
    M̂
M̂                                                                       20
x0=[0;0];   %initial conditionsM̂
str=[];   % stringM̂
ts=[0 0;T 0]; % smapling (time,offset) pair for continuous and discrete statesM̂
set_param(gcb,'UserData',x0(1)); % initialize to store state no. 1 in UserDataM̂
M̂
elseif abs(flag)==1 % return derivatives of statesM̂
        M̂
    dx(1,1)=u(1)^2; % integral of relative delection of cantilever wrt M̂
    %piezo to be used in computing rms oscillation amplitudeM̂
    sys=dx;M̂                                                            30
```

```
  M̂
elseif flag == 2  % update discrete stateM̂
  M̂
  if u(5)==1 M̂
    M̂
    nn=nn+1;M̂
   if nn==60M̂
   u_prev=get_param(gcb,'UserData');M̂
M̂
                sys=sqrt((x(1,1)− u_prev(1,1))/(t−TT1));M̂                    40
    M̂
    set_param(gcb,'UserData',x(1,1));M̂
    M̂
    nn=0;M̂
    TT1=t;M̂
    endM̂
 endM̂
  M̂
M̂
elseif flag == 3        % returns system states as outputs in vector sysM̂      50
  M̂
M̂
vel_in = x_s/D∗omega_d/omega∗cos(omega_d/omega∗t); %effective shaker velocityM̂
y_bi= x_s/D∗sin(omega_d/omega∗t); % position of bimorph relative to piezo tube free endM̂
delta=(l_t/D+u(6)−u(2)−u(1)−y_bi);M̂
M̂
if delta>0.995∗delta_o,M̂
  if u(7)==0M̂
    t_c=t;M̂
  elseM̂                                                                      60
    t_c=u(7);M̂
  endM̂
```

```
% Initial guessM̂
    m=25;M̂
    aa=25;M̂
    %initializeM̂
    i=1;M̂
    f(i)=1; g(i)=1; dm(i)=1; da(i)=1;M̂
M̂
    while abs(f(i))>=1e-8 & abs(g(i))>= 1e-8 & abs(dm(i))>=1e-8 & abs(da(i))>=1e-8
    i=i+1;   M̂
    f(i)=lambd*aa^2/2*( sqrt(m^2-1)+(m^2-2)*asec(m)) + 4*lambd^2*aa/3*(1-m+sqrt(m
    dfda=lambd*aa*( sqrt(m^2-1)+(m^2-2)*asec(m) )+ 4/3*lambd^2*( 1-m+sqrt(m^2-1)
        dfdm=lambd*aa^2/2*( m/sqrt(m^2-1) + 2*m*asec(m)+(m^2-2)/m/sqrt(m^2-1
        4/3*lambd^2*aa*(-1+m*asec(m)/sqrt(m^2-1)+1/m);M̂
        % imposing delta as the known variableM̂
        g(i)=aa^2-4*lambd*aa/3*sqrt(m^2-1)-delta;M̂
        dgda=2*aa - 4/3*lambd*sqrt(m^2-1);M̂
        dgdm=-4/3*lambd*aa*m/sqrt(m^2-1);M̂
        %solving system of linear algebraic equations M̂                    80
        DFG=[dfda dfdm;dgda dgdm];M̂
        B=[-f(i);-g(i)];M̂
        dadm=DFG\B;M̂
        da(i)=dadm(1);M̂
        dm(i)=dadm(2);M̂
        aa=aa+da(i);M̂
    m=m+dm(i);M̂
    cc=m*aa;M̂
    bb=aa+n*(cc-aa);M̂
    endM̂                                                                   90
    P=aa^3-lambd*aa^2*( sqrt(m^2-1) +m^2*asec(m));M̂
    P_damp= -(b_cont*(u(3)+u(4)+vel_in))/pi/R/w;M̂
M̂
elseif delta <=0.995*delta_o, M̂
```

```
    t_c=0;M̂
    P=P_o*(delta_o+zeta_o)^2/(delta+zeta_o)^2;M̂
    P_damp=0;M̂
    m=0;M̂
    bb=0;M̂
end M̂                                                    100
    M̂
        y_rms=x(2,1); M̂
        y_s=u(6);M̂
        sys=[P_damp;M̂
      P;M̂
      bb;M̂
        y_s;M̂
        y_bi;M̂
      delta;M̂
      y_rms;M̂                                            110
      t_c];M̂
else M̂
      sys=[ ];M̂
end
```

D.4 Findz Function

```
function [sys,x0,str,ts]=findz(t,x,u,flag,e,z_o,eV_J,w,R,lambda_f,settle)M̂
global nn TT1M̂
% %  Written by: Amro M. Farid M̂
%  Program name: findz                                    M̂
%  Date: 4/22/2000 M̂
% M̂
M̂
if flag==0    % return structure and initial conditionsM̂
   sizes=simsizes;M̂
   sizes.NumContStates=0;M̂                                                    10
   sizes.NumDiscStates=0;M̂
   sizes.NumOutputs=2;M̂
   sizes.NumInputs=2;M̂
   sizes.DirFeedthrough=1;M̂
   sizes.NumSampleTimes=1;M̂
   M̂
   sys=simsizes(sizes);M̂
M̂
        x0=[];                                    %initial conditionsM̂
        str=[];                                   % stringM̂                  20
        ts=[0 0];                                 % smapling (time,offset) pair for continuous a
elseif flag ==1M̂
   sys=0;M̂
elseif flag == 3              % returns system states as outputs in vector sysM̂
   if u(2)==0M̂
      fn=0;M̂
   elseM̂
      fn=u(1);M̂
   end  M̂
   if fn==0M̂                                                                  30
```

```
        z=0;
        Fstar=0;
    else
    fn=fn*pi*w*R;
    es=num2str(e*eV_J);
    zos=num2str(z_o);
    fns=num2str(fn);
    func=['24' es '*(2*(x.^13)-(x.^7))-' fns '*' zos];
    a=fzero(func,1,1e-6);
    z=z_o/a;
    Fstar=4*e*(a^12-a^6)*eV_J*2*pi/lambda_f;
    end
    sys=[z; Fstar];
else
    sys=[ ];
end
```

D.5 Finds Function

```
function [sys,x0,str,ts]=finds(t,x,u,flag,kc,lambda_f)M̂
global nn TT1M̂
% %  Written by: Amro M. Farid M̂
%  Program name: finds                                    M̂
%  Date: 4/22/2000 M̂
% M̂
M̂
if flag==0   % return structure and initial conditionsM̂
   sizes=simsizes;M̂
   sizes.NumContStates=0;M̂                                                    10
   sizes.NumDiscStates=0;M̂
   sizes.NumOutputs=1;M̂
   sizes.NumInputs=3;M̂
   sizes.DirFeedthrough=1;M̂
   sizes.NumSampleTimes=1;M̂
   M̂
   sys=simsizes(sizes);M̂
M̂
        %x0=[0 0];                                    %initial conditionsM̂
        str=[];                                       % stringM̂                 20
        ts=[0 0];                                     % smapling (time,offset) pair for continuous a
elseif flag ==1M̂
   sys=0;M̂
elseif flag == 3              % returns system states as outputs in vector sysM̂
   if u(3)==0M̂
      s=0;M̂
   elseM̂
      kcstring=num2str(u(3)/(kc*lambda_f));M̂
      YminusX=num2str(u(1));M̂
      func=[YminusX '-x-sin(2*pi*x)*' kcstring];M̂                              30
```

```
    s=fzero(func,u(2),1e-6);
  end
  sys=s;
else
  sys=[];
end
```

Appendix E

Contact Mode Simulation with True Lateral Natural Frequency

In Chapter 5, the lateral natural frequency was decreased by a factor of thirty to illustrate the oscillation of the cantilever after a slip event. This appendix shows the results obtained from maintaining the the actual value of the natural frequency. Figure E-1 shows the results analagous to Figure 5-4

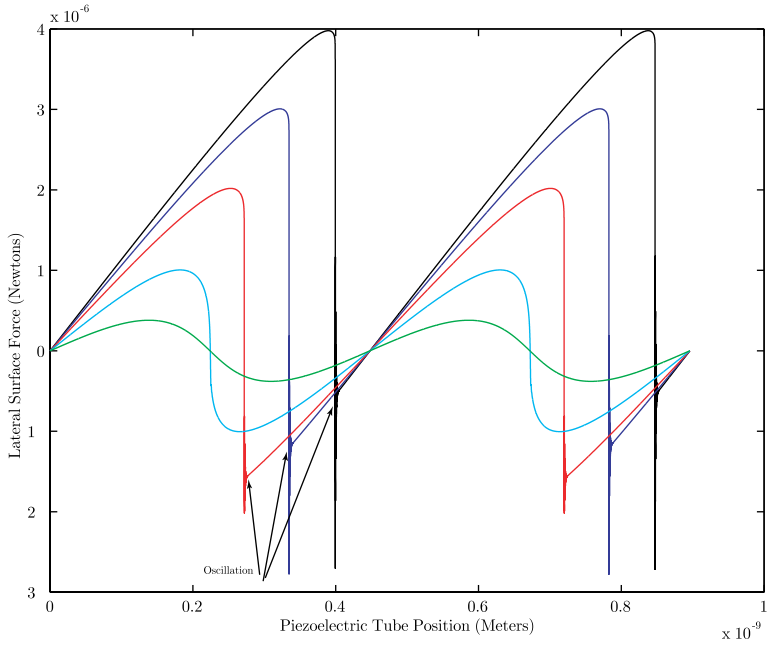

Figure E-1: Results of Lateral Surface Force Simulations for Five Cantilever Deflections

Three arrows point to the oscillation in the three unstable friction traces. As can be seen, the oscillation damps out much faster than previously shown. This is an important point because the fast decay time would probably lead to the oscillation being undetected in experimental friction measurments. Nevertheless the oscillation would occur resulting in possible damage to the sample surface.

Bibliography

[1] Binnig, G. *Physical Review Letters* vol. 56. p930-933. 1986.

[2] Carpick, Robert W. and Salmeron, Miquel. *Chemistry Review* vol. 97. p1163-1194. 1997.

[3] http://www.di.com

[4] Quist et al. *Scanning Microscopy* vol. 9. p395. 1995.

[5] Maivald, P. et al. *Nanotechnology* vol. 2 p.103-106. 1991.

[6] Burham, N.A. and Colton, R.J. *Journal of Vacuum Science Technology* vol. A7. p.2906. 1989.

[7] Ohara, Tetsuo and Youcef-Toumi, K. *Proceedings of the American Control Conference.* vol. 5 num. 95CH35736. p3808-3812. 1995.

[8] Rao, Singiresu S. *Mechanical Vibrations. 3rd ed.* Addison Wesley Publishing Company. Reading, Massachusetts. 1995.

[9] Ashby, M.F. *Materials Selection in Mechanical Design* Reed Elsevier Publishing. Oxford. 1992.

[10] Bowden, F.P. and Tabor, D. *The Friction and Lubrication of Solids.* Oxford University Press. Oxford. 1950.

[11] Lovell, M.R. et al. *Journal of Tribology* vol. 118 num. 4 p858-864. 1996.

[12] Lantz, M.A. et al. *Physical Review B-Condensed Matter* vol. 55 num. 16 p10776-10785. 1997.

[13] Burns, A.R. et al. *Langmuir* vol. 15. num. 8 p2922-2930. 1999.

[14] Johnson, K.L et al. *Proceedings of the Royal Society of London A*.vol. 32 num 324 p.301-313 1971.

[15] Carpick, R.W et al. *Journal of Vacuum Science Technology B.* vol. 14 num 2. p.1289-1295. 1996.

[16] Maugis, Daniel *Journal of Colloid and Interface Science* vol. 150 num. 1 p243-269. 1992.

[17] Johnson, K.L. and Woodhouse, J. *Tribology Letters.* vol. 5. num 2-3. p.155-160. 1998.

[18] Dedkov, G.V. *Materials Letters* vol. 38. num. 5. p360-366. 1999.

[19] Brown, Theodore L. *Chemistry: The Central Science. 7th ed.* Prentice Hall. Upper Saddle River, New Jersey. 1997.

[20] Landman, Uzi et al. *Surface Science* vol. 210. p.L-177. 1989.

[21] Buldum, A. and Ciraci, S. *Physical Review B.* vol. 55. num 4. p2606-2611. 1997.

[22] Gyalog, Tibor and Thomas, Harry. *Zeitschrift Fur Physik B- Condensed Matter.* vol. 104. num 4. p669-674. 1997.

[23] Zhong, W. and Tomanek D. *Physical Review Letters* vol. 64. num 25. p3054-3057. 1990.

[24] Tomanek, D. et al. *Europhysics Letters* vol. 15. num 8. p887-892. 1991.

[25] Baumberger, T. *Physical Review B-Condensed Matter.*. vol. 60. num 6. p3928-3939. 1999.

[26] Dankowicz, H. *Zeitschrift Feur Angewandte Und Mechanik.* vo. 19. num 6. p399-409. 1999.

[27] El Rifai, Osamah and Youcef-Toumi, Kamal. Dynamics of Atomic Force Microscope. Mechatronics Research Laboratory. Report No. MRL 00-001, Massachesetts Institute of Technology. 2000.